Developments in the Built Environment 19 (2024) 100486

Contents lists available at ScienceDirect

Developments in the Built Environment

journal homepage: www.sciencedirect.com/journal/developments-in-the-built-environment

# Self-healing concrete with a bacteria-based or crystalline admixture as healing agent to prevent chloride ingress and corrosion in a marine environment

Vanessa Giaretton Cappellesso [a,b], Tim Van Mullem [a], Elke Gruyaert [b], Kim Van Tittelboom [a], Nele De Belie [a,*]

[a] Magnel-Vandepitte Laboratory, Department of Structural Engineering and Building Materials, Faculty of Engineering and Architecture, Ghent University, Technologiepark Zwijnaarde 60, B-9052, Ghent, Belgium
[b] KU Leuven, Department of Civil Engineering, Materials and Constructions, Ghent Technology Campus, Gebroeders De Smetstraat 1, B-9000, Ghent, Belgium

ARTICLE INFO

*Keywords:*
Self-healing concrete
Healing agents
Corrosion
Chloride
Marine environment
Concrete durability

ABSTRACT

Innovative solutions are needed to improve the durability of concrete structures in marine environment. Bacteria-based agents (BAS) and crystalline admixtures (CA) are explored as healing agents to enhance chloride resistance and prevent corrosion. Healing of 100 μm and 300 μm wide cracks was investigated, in combination with two conditioning methods. Either the samples were subjected to wet/dry cycles for 3 months before exposure ("healed"), or they were directly exposed to artificial seawater after crack creation ("unhealed"). After 12 months of submersion, BAS reduced chloride ingress even in the presence of cracks but showed limitations in preventing corrosion in cracked samples. In contrast, the CA series demonstrated a reduction in chloride ingress in both uncracked and cracked concrete and effectively prevented reinforcement corrosion in healed samples and samples with cracks of 100 μm. This highlights the potential of customized self-healing solutions to improve concrete durability in marine environments.

## 1. Introduction

The durability of concrete structures in marine environments has always been a major concern. The combination of chloride and sulfate ions in seawater can trigger various degradation mechanisms (Alexander et al., 2013), such as the formation of concrete cracks and reinforcement corrosion, which can undermine the structural integrity of marine structures such as offshore installations, piers, bridges, and tunnels (Cappellesso et al., 2023a). Researchers and experts have emphasized the profound impact of seawater on concrete durability (Maes, 2015; Kušter Marić et al., 2020; Santhanam and Otieno, 2016; De Weerdt et al., 2014). However, the complex interplay of environmental factors further complicates this scenario. Concrete structures in marine environments are susceptible to deterioration mechanisms depending on exposure zones. Airborne chlorides instigate chloride-induced corrosion, predominantly observed in atmospheric environments. Conversely, in splash or tidal zones, processes such as diffusion, sorption, and permeation exert notable influences. In fully submerged conditions, impermeability becomes paramount, given the pivotal roles of factors such as permeation and diffusion. Seawater contains various ions and compounds that can react with concrete components under certain conditions. For instance, magnesium ions ($Mg^{2+}$) in seawater can react with calcium hydroxide ($Ca(OH)_2$) in concrete to form brucite ($Mg(OH)_2$). Similarly, calcium ions ($Ca^{2+}$) can react with carbonate ions ($CO_3^{2-}$) in seawater to form aragonite ($CaCO_3$). Seawater salinity varies (Yi et al., 2020), but chloride ions are prevalent, in addition to sulfates coming from $MgSO_4$ (Biczok, 1967; Mehta et al., 1999). Deterioration also depends on multiple environmental factors. Seawater can react with concrete resulting in a double layer of gypsum and brucite. Dissolved $CO_2$ in seawater can form a layer of aragonite acting as a temporary barrier to seawater ingress (De Weerdt et al., 2014). The combination of gypsum with calcium aluminates can create ettringite, mitigating concrete damage (Mehta, 1991). Yet, this is influenced by chloride binding which can reduce ettringite formation by reducing the availability of calcium aluminates (Verbeck, 1975).

The diffusion of chlorides initially decreases when there is a higher amount of sulfate present (Wu et al., 2020). This is because the reaction products related to sulfate attack, such as gypsum and ettringite, are

* Corresponding author.
*E-mail address:* nele.debelie@ugent.be (N. De Belie).

https://doi.org/10.1016/j.dibe.2024.100486
Received 15 February 2024; Received in revised form 30 May 2024; Accepted 19 June 2024
Available online 21 June 2024

more voluminous and obstruct the pore network (Ramezanianpour et al., 2021). However, in the final stage, the diffusion of chlorides in the presence of sulfates increases again because the continued growth of the expansive reaction products, caused by sulfate attack, leads to crack formation. Studies have confirmed that when there is a combined sulfate-chloride attack, the damage is aggravated because the cracking process becomes increasingly severe and opens paths for chloride ion penetration (Zhao et al., 2020). According to Kušter Marić et al. (Kušter Marić et al., 2020), cracks larger than 100 μm can significantly decrease the time for depassivation, regardless of the thickness of the cover zone. Corrosion caused by marine exposure is worsened in case of wider cracks varying from 250 to 500 μm, according to Montes et al. (2004). Otieno et al. (2016) found that thick concrete covers can prevent corrosion in narrow cracks. However, for wider crack widths of 400–700 μm, the cover thickness has little effect. Lopez-Calvo et al. (2018) observed that the risk of corrosion increased with increasing crack width in a simulated marine tidal condition, but this risk can be reduced by increasing the cover thickness. Du et al. (2020) discovered that it takes 700 days to initiate corrosion in cracked samples with a crack width of 100 μm, while this was reduced to 460 days for cracks of 300 μm. Lv et al. (2021) found that even cracks around 50 μm wide become rich in chloride ions, leading to small additional cracks in the surrounding matrix.

Self-healing technologies have emerged as a promising solution to combat this degradation and extend the service life of marine concrete structures (Cappellesso et al., 2023a). Self-healing is gaining traction as a solution to the challenges of sustainable infrastructure (Li and Herbert, 2012; De Belie et al., 2019). This approach involves incorporating healing agents into concrete to give the matrix self-repair capabilities, reducing the impact of cracks, and preventing corrosion (Palin et al., 2017; Cappellesso et al., 2023b; Erşan et al., 2018), making it ideal for concrete structures in marine environments. Academic research often focuses on the effects of one single aggressive agent, but only a few studies have examined the impact of combined attacks (Lv et al., 2021; Zhang et al., 2023; Wu et al., 2023; Khan et al., 2021a, 2021b; Zhan et al., 2022) on self-healing concrete. Studies were conducted to investigate the self-healing capacity of UHPC made with different types of cement (CEM I and CEM III) with crystalline admixture (CA), along with specific nano-additions (alumina nanofibers and cellulose nanocrystals and nanofibrils) (Cuenca et al., 2021a, 2021b; Lo Monte and Ferrara, 2020). The concrete was exposed to natural geothermal water containing chlorides and sulfates, with tests performed in permanent immersion and wet/dry cycles up to six months. Results showed that UHPC made with CEM III showed better self-healing performance than UHPC with CEM I, although the differences were less significant upon multiple re-cracking and for longer exposure times. Xue (2022a) found that the type of CA used in concrete exposed to seawater affects its self-healing performance. Seawater reduces chloride ingress due to brucite precipitation in cracks (Xue, 2022b). He et al. (2020) incorporated a non-commercial CA into mortar exposed to seawater and achieved complete healing of cracks up to 350 μm, while exposure to freshwater only resulted in healing of cracks up to 240 μm. Brucite and calcium carbonate were identified as healing products in the cracks (He et al., 2020). When using bacteria-based self-healing concrete, it is important to select bacteria that can survive in seawater. Palin et al. (2017) developed a bacteria-based self-healing cementitious composite for low-temperature (8 °C) marine environments. The agent can heal 95% of 400 μm wide cracks and 93% of 600 μm wide cracks (Palin et al., 2017). Khan et al. (2021a) used spores of *Sporosarcina halophila* bacteria, calcium lactate, and expanded perlite aggregate as the carrier in mortar exposed to submerged and tidal marine environments for 90 days. Bacteria, water, and oxygen led to aragonite and brucite formation, resulting in 50% crack closure for cracks up to 800 μm (Khan et al., 2021a). In a similar study the same authors. Khan et al. (2021b) considered another type of bacteria, *Halobacillus halophilus*, which lead to aragonite and brucite formation improving by 17% the autonomous healing of concrete under both submerged and tidal marine conditions. Zhan et al. (2022) prepared pastes with *Bacillus mucilaginosus* bacteria to be tested under simulated marine condition considering 500 μm-wide cracks. The authors identified healing products in the crack by μCT, showing no uniform distribution but rather a range of healing ratios between 50% and 95% depending on the section analysed (Zhan et al., 2022). Most studies focus on mesoscale analysis, involving experiments with pastes or mortar. However, there is a noticeable gap in the literature regarding macroscale analysis, which involves concrete samples.

This paper presents a new approach to the use of self-healing concrete in marine environments. It examines the effectiveness of two commercial healing agents - a bacteria-based (BAS) and a crystalline admixture agent (CA) - in pre-cracked concrete specimens with two different crack widths (100 μm and 300 μm). These specimens were exposed to simulated marine conditions for one year, which included most common salts found in seawater to make the results more realistic. Unlike most literature on the subject, this study prioritizes durability over visual examination of crack closure. Chloride penetration, mass change, corrosion, and microanalysis were performed to obtain more accurate results. By investigating the impacts of sulfate and chloride ion ingress, along with other degradation factors, this research provides valuable insights into the durability of self-healing concrete in challenging marine environments.

## 2. Materials and methods

### 2.1. Materials

The applied cement type was Portland cement CEM I 52.5 N. The company Holcim Group provided the chemical composition presented in Table 1. The fine aggregate used was a sand with grading between 0 and 4 mm, where the estimated fineness modulus amounted to 2.92. For the coarse aggregates rounded gravel was used with a grading between 2 and 8 mm. A pure limestone filler was considered with 0.99 g of $CaCO_3$ for every gram of limestone filler. The particle size distributions of fine and coarse aggregates together with the limestone filler are shown in Figure S1 (Supplementary material). A liquid superplasticizer was used (MasterGlenium 27, Master Builders Solutions) that has a density of 1.05 g/cm$^3$, a pH of 7, and a solid content of 20%.

The crystalline admixture (CA), named Penetron ADMIX, was provided by Penetron, Italy. It is a commercially available agent with waterproofing features combined with a self-healing ability defined as permeability-reducing admixture for hydrostatic conditions (PRAH) by ACI 212 (2016). The composition consists primarily of Portland cement and chemicals (65–80%), along with CTS-15-1 (10–30%) and CTS-15-2 (5–10%). Additionally, it includes calcium magnesium hydroxide (1.5–6%), calcium magnesium hydroxide oxide (1.5–6%), and calcium hydroxide (1.0–2%). The compounds CTS-15-1 and CTS-15-2 are kept as a trade secret. The suggested dosage for concrete compositions is between 0.8 and 1% of the cement weight. In this research 0.8% of the cement weight was used. The product is applied as an admixture, and it is added to the dry materials during concrete mixing. Related to the physical properties, the density of the CA is 2.73 kg/dm$^3$. It has a grey powder appearance, is odorless and has a pH of 10–13 for a 10% solution in water. Bacteria embedded into polylactic acid capsules were used as a bacteria-based healing agent (BAS) to provide the concrete with self-healing properties. It is a commercial product supplied by Green-Basilisk B.V., the Netherlands. The composition includes PLA at 50–80%, bacterial spores at 0.1–2%, nutrients such as calcium lactate at 10.5–43%, and moisture at 1–5%. The healing agent is available in powder form and is composed of bacterial spores (*Bacillus cohnii*) and calcium lactate as a calcium source (Mors and Jonkers, 2020; He et al., 2023; Rossi et al., 2022; Rodríguez et al., 2020). Both are pelletized through extrusion of the calcium source and the bacterial spores, followed by grinding of the extrudate. The capsules have a particle size distribution between 0.1 and 1.0 mm with a density of 1200 kg/m$^3$. The pellets are manufactured from a PLA derivate matrix, bacterial spores

**Table 1**
Chemical composition of the cement CEM I 52.5 N. (LOI: loss on ignition @1000 °C).

| Composition | CaO | $SiO_2$ | $Al_2O_3$ | $Fe_2O_3$ | MgO | $Na_2O$ | $K_2O$ | $SO_3$ | $Cl^-$ ion content | LOI | Insoluble residue |
|---|---|---|---|---|---|---|---|---|---|---|---|
| Result (%) | 64.3 | 18.3 | 5.2 | 4.0 | 1.4 | 0.32 | 0.43 | 3.5 | 0.06 | 2.3 | 0.4 |

with limestone powder, nutrients and water (Rodríguez et al., 2020; Basilisk-Contracting, 2019). The bacteria-based concrete, depending on the dosage of the healing agent, can heal cracks up to 0.8 mm under laboratory conditions (Mors and Jonkers, 2020). The recommended healing agent dosage is 5–15 kg/m$^3$ of concrete. This study investigates a dosage of 10 kg/m$^3$.

### 2.2. Concrete mix properties and sample preparation

Table 2 contains information on the composition of the concrete mix, including its properties in both the fresh and hardened state. This table compares the reference concrete (REF) with concrete that contains either the crystalline admixture (CA) or the bacteria-based healing agent (BAS). Standardized procedures provided by EN 12350-7 (EN 12350-7, 2019) were followed to determine air content, and guidelines specified in EN 12350-6 (EUROPEAN COMMITTEE FOR STANDARDIZATION, 2019) were used to assess fresh density. The flow behavior of the concrete was evaluated according to EN 12350-5 (EN 12350-5, 2019). The observed increase in flow of BAS compared to REF, as recorded in Tables 2 and is likely due to BAS's distinct physical and chemical characteristics, such as particle size distribution and surface morphology, as well as possible additives or modifications that enhance its flowability. Additionally, environmental factors like humidity and temperature during testing may have differentially impacted the flow behavior of BAS and REF, warranting further investigation into their physico-chemical properties and rheological behavior. The compressive strength was determined from three 150 mm cubes in accordance with EN 12390-3 (EN 12390, 2019).

For the mixing procedure, the dry materials were added to the mixer and mixed for 1 min, then the water with the superplasticizer was added, and mixing was continued for three more minutes. The healing agents were added together with the dry materials. The preparation of reinforced prismatic specimens (60 x 60 x 220) mm$^3$, reinforcement details see below) was performed using a planetary mixer with a 50 L capacity and rotating pan (Eirich, Germany). The concrete was poured into the molds in two layers, each vibrated on a vibration table for 10 s. After casting, the specimens were stored in an air-conditioned room (at 20 ± 2 °C and ≥95% relative humidity) for 24 h. Subsequently, samples were demolded and placed in the same curing room until cracks were created.

Three-point bending was utilized to induce cracking at 28 days. In this study, notches were not used. Crack widths were controlled using a Linear Variable Differential Transformer (LVDT) positioned at the bottom of the specimens, fixed on metal plates, which were attached to the sample at a distance of 35 mm from the middle (Figure S2 - Supplementary material). A Walter-bai testing machine with capacity of 15 kN was used to control the load with the LVDT at a constant rate of 0.0007 mm/s. The study included two intended crack widths, namely 100 μm and 300 μm, the width of the final crack before unloading was 290 μm and 480 μm, respectively.

**Table 2**
Concrete mix composition and properties in fresh and hardened state.

| Materials [kg/m$^3$] | REF | CA | BAS |
|---|---|---|---|
| CEM I 52.5 N | 340.0 | 339.7 | 337.1 |
| Sand 0–4 mm | 748.1 | 747.6 | 741.8 |
| Gravel 2–8 mm | 1038.3 | 1037.6 | 1029.5 |
| Limestone filler | 58.4 | 58.4 | 57.9 |
| Crystalline admixture | – | 2.7 | – |
| Bacteria-based agent | – | – | 10.0 |
| Water | 170.0 | 169.9 | 168.5 |
| Superplasticizer | 2.2 | 2.2 | 2.2 |
| **Fresh Properties** | | | |
| Density [kg/m$^3$] | 2387.5 | 2350.0 | 2343.8 |
| Air content [%] | 2.8 | 2.0 | 2.5 |
| Flow [mm] | 540 | 520 | 560 |
| **Hardened properties at 28 days** | | | |
| Compressive strength [MPa] | μ: 54.4<br>CV: 1.2% | μ: 60.4<br>CV: 2.7% | μ: 61.6<br>CV: 0.7% |

Two types of reinforcement were considered, one for the submerged condition with a focus on the ingress of aggressive agents in the concrete, and another specifically to monitor corrosion. The reinforcement used for the experiments focusing on measuring the ingress of aggressiveness consisted of two smooth copper-coated steel wires of 2 mm in diameter placed at the bottom of the formwork, each spaced 10 mm from the respective sides and bottom of the mold. The prisms were sawn after crack creation, reducing their length from 220 mm to 80 mm, keeping the crack in the middle. The outer parts with the length of 70 mm which were sawn off were used as uncracked reference specimens. For the corrosion monitoring one smooth reinforcement steel bar with a diameter of 5.6 mm was centrally positioned 20 mm away from the bottom surface. Following the creation of cracks, the samples were sawn, reducing their length from 220 mm to 50 mm, while keeping the crack in the middle. The portions removed from the sides during sawing were utilized as uncracked specimens after they were sawn to the same dimension as the cracked samples.

The experiment to measure the ingress of aggressive agents consisted of ten uncracked samples, ten samples with cracks of 100 μm in width and ten samples with cracks of 300 μm in width. In case of the corrosion experiment, each series involved the analysis of three uncracked samples, four samples with a crack width of 100 μm, and four samples with a crack width of 300 μm.

The healing regime consisted of three months of a cyclic wet-dry condition (4 days wet/3 days dry) using demineralized water. The samples subjected to the healing regime had the exposed edges of the reinforcement bars sealed with white silicone before the beginning of the healing process. This sealing acted as a protective measure to prevent corrosion of the reinforcement from the sides of the samples during the healing regime. However, it is worth noting that water ingress from the cracks could still have a preliminary influence on the corrosion of the reinforcement, although this is an inherent challenge even in real-world scenarios. In the case of unhealed samples, to guarantee the same age at the beginning of the experiment, they were placed in a standard laboratory condition (20 °C, 60% RH) for the equivalent time of the healing regime.

Related to the sample preparation before exposure, the samples used for the experiments focusing on measuring the ingress of aggressive agents were coated with an epoxy resin, named Episol® Designtop SF, used to prevent contact between the samples' sides and the aggressive environment. Two layers were applied considering a minimal interval of 4 h between them. Only the surface where the crack was located was left uncoated, i.e., five out of six sides were coated for the prisms. The uncracked samples used as a control were coated in the same way as the cracked samples. However, the samples used for mass control (test described in Section 2.4) were kept uncoated to guarantee the attack from all surfaces. For the mass control test, ten samples were prepared per each series.

The sample preparation for the corrosion experiment was conducted following the methodology outlined in the Erşan et al. (2018) study. To prepare the samples for the corrosion experiment, a 15 mm wide aluminum butyl tape was applied to the lateral surfaces at the lower part of the sample that would be in contact with seawater, where the crack

was located. This procedure was performed to seal the edges of the surface in contact with the marine solution, allowing for unidirectional ingress. The aluminum butyl tape was employed to also cover one exposed end of the reinforcement bars at the smaller side surface of the sample. At the opposite end of the reinforcement, an insulated copper wire was connected to create an electrical connection between the steel rebar and the data logging system. The wire was protected with non-conductive tape. Furthermore, a 5 mm thick sheet of colorless plastic material was attached to all side surfaces using superglue. To ensure thorough protection, the corners of the samples were taped off, and silicone was applied to the edges of the top and bottom surfaces to prevent solution absorption from the sides. These preparations were crucial for safeguarding the samples against corrosion on the side surfaces. Only the bottom surface, in contact with the seawater solution, and the top cast surface remained unprotected. The exposed top surface allowed to control drying of the samples, preventing them from becoming fully saturated. A schematic drawing in Fig. 1 is presented to provide a clearer understanding of the sample preparation process.

### 2.3. Laboratory-scale simulation of marine environments

Samples for measuring the ingress of aggressive agents were completely submerged in an artificial seawater solution for one year. For this condition, a ratio of 80 between the exposed concrete surface area ($cm^2$) and the volume of the solution ($dm^3$) was considered (NT Build 443, 1995). The specimens were immersed in the test solution, with no replacement of the solution taking place. To ensure the stability of the testing environment, both pH and sulfate concentration were regularly monitored. Specifically, the pH of the solutions was carefully controlled over time and maintained within the range of 7.8–8.5. This was achieved by regular pH measurements using a calibrated pH meter. The results indicated that no adjustments were necessary to keep the pH within this range, suggesting that the solution composition remained stable throughout the experiment. Moreover, the ratio between the volume of the solution and the surface area of the specimens was sufficiently large. This ensured that the solution's properties did not undergo significant changes during the experiment.

In contrast, samples for corrosion measurements were placed on spacers and artificial seawater solution was added until the level was 5 ± 3 mm above the bottom of the samples. This resulted in an absorption-based transport mechanism, and the seawater was renewed every two weeks to maintain stable salt concentrations throughout the corrosion experiment. For samples with cracks, they were positioned with the crack in the bottom cast surface facing downward. The equivalent surface was used for uncracked samples. The samples were pre-saturated through submersion in demineralized water for two days before being brought into contact with the seawater solution. The containers with solution were kept in an air-conditioned room (20 °C, 60% RH). The composition of the solution is prescribed in ASTM D1141-98 (ASTM D1141 − 98, 2021) and shown in Table 3. Demineralized water was used to prepare the solutions.

**Table 3**
Artificial seawater (ASTM D1141 − 98, 2021).

| Compound | Concentration [g/L] |
|---|---|
| NaCl | 24.53 |
| $MgCl_2$ | 5.2 |
| $Na_2SO_4$ | 4.09 |
| $CaCl_2$ | 1.16 |
| KCl | 0.695 |
| $NaHCO_3$ | 0.201 |
| KBr | 0.101 |
| $H_3BO_3$ | 0.027 |
| $SrCl_2$ | 0.025 |
| NaF | 0.003 |

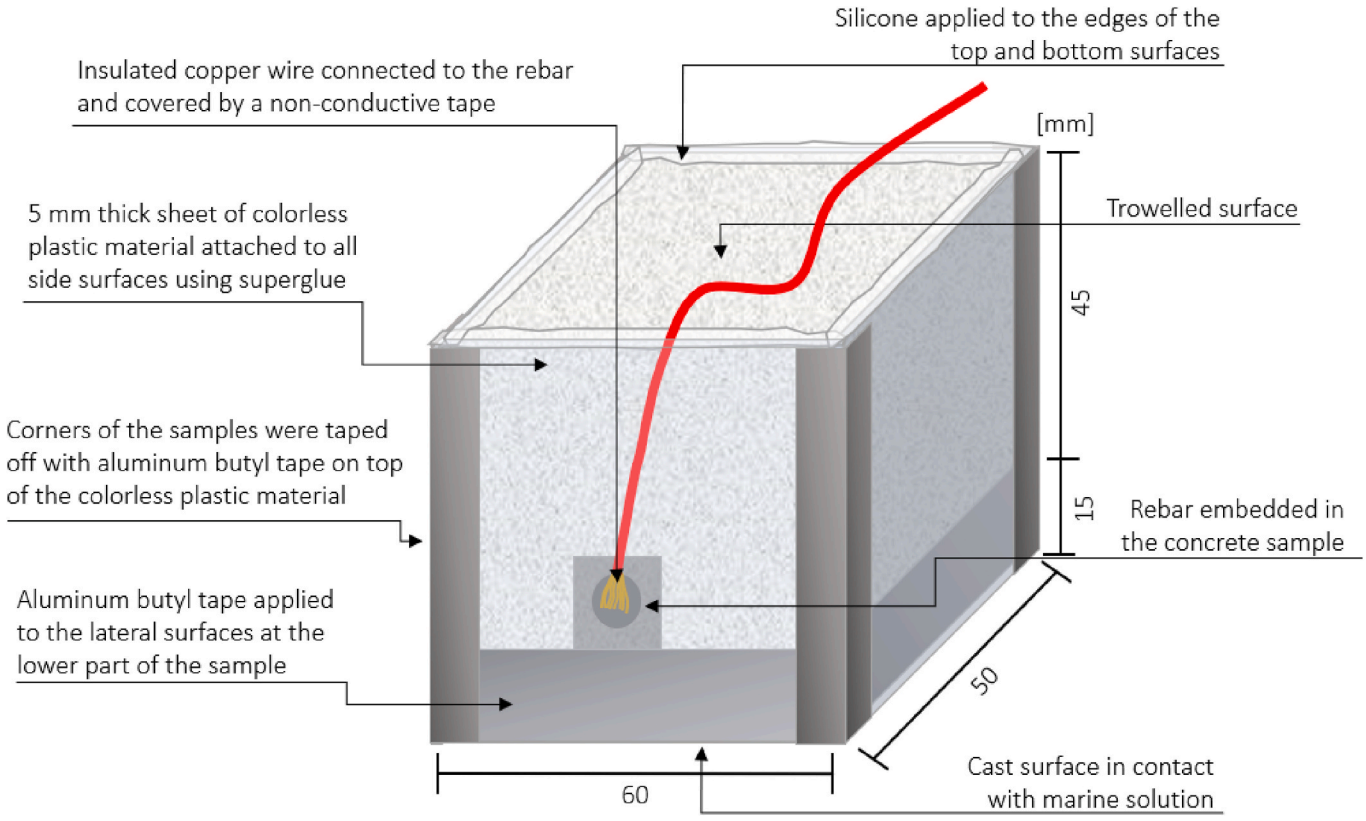


**Fig. 1.** Scheme of the sample preparation for the corrosion experiment in marine environment.

### 2.4. Test methods related to aggressive agent ingress

#### 2.4.1. Crack width and crack closure analysis

Microscopic images were taken to evaluate the crack width and crack closure obtained for each series. The measurements were executed with a stereomicroscope, Leica S8 APO, with DFC 295 camera. The crack width was measured in up to six predetermined places taken along the crack length with five measurements per location on the surface of the specimens in contact with the seawater solutions. In this way, at least 20 measurements were taken per sample. For the healed series the self-healing efficiency (SE) in percentage was calculated considering the measurements before and after application of the healing regime, using Equation (1). CW represents the average crack width per specimen (i) either at the time zero ($t_0$) right after crack creation, or after healing ($t_{healed}$).

$$SE\,[\%] = \frac{CW_i^{t_0} - CW_i^{t_{healed}}}{CW_i^{t_0}} \times 100\% \qquad \text{Equation 1}$$

#### 2.4.2. Chloride penetration tests

In this research, to detect chloride penetration, silver nitrate spraying was used after 1, 3, 6 and 12 months of exposure in the marine solution. Additionally, the chloride ion content was evaluated through titration after 3 and 12 months. The titration after 3 months of exposure was conducted on both cracked and uncracked samples, by analyzing the total chloride content. After 12 months of exposure, only uncracked samples were considered. Additionally, free chloride analysis was conducted. On the day of the analysis, three separate samples were tested for chloride ingress through the color change boundary condition, while the chloride content analysis was performed for one concrete sample. To determine the ingress depth of chlorides into the concrete, the fractured sample halves were split perpendicular to the crack surface and uncracked samples followed the same procedure. A solution of 0.1 mol/L silver nitrate was sprayed on the specimens, which made the chloride-contaminated area appear lighter. Nine measurements were taken for uncracked concrete, with the first measurement starting 10 mm from the specimen's side, and a 10 mm gap between each measurement. For cracked specimens, measurements were taken every 5 mm in the central zone of 40 mm that contained the crack, and every 10 mm in the two outer zones of 30 mm. Chloride ingress was measured for a total of thirteen points in cracked samples.

The acid-soluble chloride titration was used to calculate the total chloride content and the water-soluble chloride titration was used to calculate the free chloride content. In summary, subtracting the free chloride content from the total chloride content allows to determine the bound chloride content, which represents the ability to bind chloride ions to hydration products. In the context of chloride-induced corrosion, a higher chloride binding capacity is desirable, primarily to reduce the presence of free chlorides that could initiate the corrosion process. Following the removal of samples from their respective environmental conditions, the samples were stored for one week in an air-conditioned room (20 °C, 60% RH) to ensure they were dry. Utilizing an automatic apparatus equipped with a 10 mm diameter diamond drill, powder was collected from the surface in layers defined according to the recommendations outlined in the EN 12390-11 (EN 12390-11, 2010) standard. This equipment allows for precise depth control at 1-mm intervals and defines the grinding area. In uncracked samples, the powders originated from the surface in contact with the salt solution. The powders extracted from the cracked specimens were collected perpendicular to the crack wall at two different heights: 15 mm and 40 mm away from the exposure surface. The powders were extracted up to a depth corresponding to the color change boundary observed in each concrete series. Table 4 presents the depth of each layer for the powder extraction procedure. Depending on the specific series, some required the extraction of powders up to layer 8, while others necessitated reaching layer 9 or even layer 11. It is worth noting that in all cases a minimum of eight layers was considered in the analysis.

**Table 4**
Depth of each layer for the powder extraction procedure.

| Layer | Depth in each layer | Accumulated |
|---|---|---|
| Layer 0 | 1 mm (discard) | 1 mm |
| Layer 1 | 2 mm | 3 mm |
| Layer 2 | 2 mm | 5 mm |
| Layer 3 | 2 mm | 7 mm |
| Layer 4 | 3 mm | 10 mm |
| Layer 5 | 3 mm | 13 mm |
| Layer 6 | 3 mm | 16 mm |
| Layer 7 | 4 mm | 20 mm |
| Layer 8 | 5 mm | 25 mm |
| Layer 9 | 5 mm | 30 mm |
| Layer 10 | 5 mm | 35 mm |
| Layer 11 | 5 mm | 40 mm |

For the acid-soluble chloride titration (total chloride content) procedure, the resulting powders underwent a drying process at 105 °C for 48 h. Subsequently, precisely 2 ± 0.001g of each powder/layer was measured in a 150 ml glass beaker. Following this, 5 ml of a 0.3 mol nitric acid solution and 40 ml of demineralized water were added. The solutions underwent stirring and were heated on a hot plate until reaching the boiling point. After cooling, filtration was carried out, and the solutions were diluted with demineralized water to a final volume of 100 mL. From these 100 mL solutions, 10 mL was pipetted and subjected to chloride concentration analysis using an automated titration equipment, the 862 Compact Titrosampler from Metrohm®. The equipment made use of 0.01 mol/L silver nitrate as the titration solution. The test solution comprised: 10 mL extract, 10 mL demineralized water, and 40 mL nitric acid (0.3 mol/L). For the water-soluble chloride titration (free chloride content) procedure, 2.5 ± 0.01g of each powder was mixed with 50 mL of demineralized water in plastic containers. The mixtures were vigorously stirred, and the containers were closed. After approximately 24 h, almost all the powders had settled at the bottom of the beakers. From the upper layer of the solution, 5 mL was extracted using a pipette. This 5 mL of extract was then combined with 15 mL of deionized water and 40 mL of nitric acid (0.3 mol/L), preparing the solutions for testing in the same automatic titration apparatus. To estimate the concrete's free chloride contents as a function of penetration depth, a factor of 0.8 was applied to the measured water-soluble chloride contents, as suggested by Yuan (2009). Finally, the chloride content ($C_t$) can be related to the weight % of the concrete according to Equation (2) (Maes, 2015; Gruyaert, 2011).

$$C_t[\text{wt.\%concrete}] = \frac{10 \bullet 35.45 \bullet 0.01 \bullet Vol(AgNO_3)}{M}.100 \qquad \text{Equation 2}$$

In this equation the dilution factor is denoted as 10, the atomic mass of chlorides is specified as 35.45 g/mol, the concentration of the titration solution is set at 0.01 mol/L, $Vol(AgNO_3)$ represents the volume of $AgNO_3$ in mL, and $M$ is the corresponding mass of the powder in kg. To adjust the chloride content in wt.% concrete to wt.% binder, Equation (3) was applied.

$$C_t[\text{wt.\% binder}] = \frac{C_t(\text{wt.\%concrete}) \bullet Density(concrete)}{Binder\ content}.100 \qquad \text{Equation 3}$$

Based on the chloride profiles obtained for each sample, the surface concentration $C_s$ (wt.% binder) and the effective chloride transport coefficient $D_e$ ($m^2/s$) were determined. This involved fitting Equation (4) to the measured chloride contents through a non-linear regression analysis. Notably, the first point of the profile, originating from the initial layer with a thickness of 1 mm, was excluded during this analysis.

$$C(x,t) = C_s - (C_s - C_0).\,erf\left(\frac{x}{2.\sqrt{D_e.t}}\right) \qquad \text{Equation 4}$$

C(x,t) represents the chloride concentration at depth $x$ and time $t$, $C_0$ denotes the initial chloride concentration, and erf(.) signifies the error function.

#### 2.4.3. Mass change tests

To assess the impact in the concrete samples of artificial seawater a series of uncracked concrete cubes with a side length of 50 mm were subjected to periodic weight measurements during exposure. These results serve to estimate the concrete's permeability when being exposed to marine conditions and potential chemical reactions that can induce mass changes over time. The mass changes were assessed for uncoated concrete cubes. To ensure accurate measurements, any excess moisture on the specimen's surface was meticulously removed using a pre-wetted cloth. A scale with 0.001 g of precision was used to verify the mass changes over time. The initial mass measurements were taken after one week of immersion in the seawater solutions. Subsequent measurements were conducted at 1, 3, 6, 9, and 12 months.

#### 2.4.4. Microanalysis

In addition, microanalysis was conducted on thin sections prepared after one year of exposure, following the procedure described in Cappellesso et al. (2023b). This analysis aimed to verify the healing products in the cracks and the effects of seawater on the surface of the concrete in the different tested series. The thin sections were analysed by light microscopy with cross polarized light (XPL). Another method used for microanalysis was Scanning Electron Microscopy (SEM) combined with Energy-Dispersive X-ray spectroscopy (EDX). This technique was used to verify the effect of the exposure condition on the concrete matrix and the healing products. A Jeol JSM-7600F Field Emission Scanning Electron Microscope equipped with AZtecEnergy software for EDX was used. Only cracked specimens were considered. In order to analyze the morphology of the products formed on the crack wall, fractured samples were analysed by secondary electrons (SEI). All the samples were coated with a platinum film with a thickness of 4 nm.

### 2.5. Corrosion experiment and test methods considered

The corrosion methodology used was based on the half-cell potential method. This is an electrochemical technique used to evaluate the corrosion potential and corrosion behavior of concrete in contact with corrosive environments, being seawater in this case. It involves setting up an electrochemical cell with a working electrode (the reinforcement bar in the concrete sample) and a reference electrode, measuring the potential difference between them.

To monitor the electrochemical corrosion potential over time, a data logging system recorded the rebar's potential relative to a saturated calomel reference electrode (SCE) for all specimens for 360 days. To ensure consistency, the samples were arranged in three separate boxes, categorized by concrete type (REF, BAS, and CA). A reference electrode was positioned centrally, and the samples were arranged in a circular pattern around it to maintain an equal distance from every sample to the electrode. During this exposure period, the samples remained uncovered in a climate room (20 °C, 60% RH). Each box was connected to a central module via equally long insulated copper wires to prevent variations in cable resistance during automatic potential measurements. The modules used were NI 9205 C Series modules from National Instruments, offering 32 available channels, each with programmable input ranges of ±200 mV, ±1 V, ±5 V, and ±10 V. The connected software was programmed to measure the potential of each individual sample every minute, and the daily average was used for plotting the data. As corrosion begins to affect the reinforcement, the breakdown of the passive layer causes an increase in potential difference measured between the electrode and the sample.

The final corrosion potential was then assessed after one year to determine the state of the reinforcement, with more negative values indicating a higher likelihood of corrosion, as outlined in ASTM C876-15 (ASTM C876-15, 2016). Potentials less negative than −126 mV indicate a 10% chance of corrosion, while those between −126 mV and −276 mV suggest approximately a 50% probability. Potentials more negative than −276 mV indicate a high 90% probability of corrosion. Note that the standard refers to potential differences derived from a standard hydrogen electrode (SHE). To ensure accurate interpretation of the results, a conversion was performed, considering the calomel electrode used in the experimental setup that has a potential (mV vs. SHE) of +244.

It is important to recognize that this isolated analysis may not always fully elucidate the actual corrosion status of the rebar (Almashakbeh et al., 2022). Therefore, a comparison in conjunction with other observations was made to validate the actual corrosion situation. Upon completion of the exposure period, the samples were extracted from their corrosive environment and subjected to a splitting test in the direction of the rebar to facilitate removal of the reinforcement bar. The rebars were carefully separated from the concrete samples for further analysis. The rebars were manually removed with the assistance of a hammer, and any corrosion products were dissolved using a chemical cleaning solution (Van Belleghem, 2018). The condition of the rebars before and after cleaning was documented through photographs. The cleaning solution, composed of HCl and $H_2O$ in a 1:1 ratio with 3 g/L of urotropine (hexamethylenetetramine), was used to fully immerse the reinforcement bars for a duration of 24 h. Subsequently, the bars were dried with paper, and their mass and length were measured. By considering the density, diameter, and length of the reinforcement, the initial mass was determined and compared with the mass after the cleaning process. This comparison provided insight into the gravimetric mass loss and allowed to correlate it with the level of corrosion within the reinforcement bars. Furthermore, at least one sample from each series underwent analysis using SEM in conjunction with EDX point analysis. This analysis aimed to determine the actual surface composition of the steel rebar in terms of $Fe_xO_y$ and Fe (wt.%). Subsequently, the surface composition of the exposed steel rebars was examined. Reductions in $Fe_xO_y$ content (wt.%) were used to distinguish the degree of corrosion in rebars taken from different series, following a method similar to that conducted by Erşan et al. (2018).

### 2.6. Overview of the experimental program

Fig. 2 provides an overview of the experimental program, detailing each step involved in the preparation, testing, and exposure of concrete specimens. This comprehensive chart illustrates the process, beginning with the preparation of different concrete mixes, followed by the preparation of specimens, number of samples and the method used for inducing cracks. It further delineates the specific preparations for evaluating the ingress of aggressive agents and monitoring corrosion, including details on reinforcement placement. Additionally, the figure outlines the conditions under which the specimens were exposed to artificial seawater, the healing regime applied, and the storage conditions for unhealed samples. This visual representation ensures a clear understanding of the methodology employed in the study.

## 3. Results and discussion

### 3.1. Analysis of the cracks

The series are described according to the specific concrete type: reference concrete (REF), concrete containing bacteria healing agent (BAS), or crystalline admixture (CA). A letter is added to indicate whether the samples were pre-conditioned in the unhealed (u) or healed (h) condition. Additionally, the presence of a crack is noted with a number: 1 for a 100 μm crack width or 3 for a 300 μm crack width. If there is no number present, it indicates an uncracked sample. Fig. 3 illustrates the crack widths observed in the analysed series for the intended crack widths of 100 μm and 300 μm. Narrow cracks showed

**Concrete type**

Reference Concrete (REF)

With Crystalline Admixture (CA)

With Bacteria-based Healing Agent (BAS)

**Specimen preparation**

Dimensions: 60 x 60 x 220 mm³

**For Ingress of Aggressive Agents**

Reinforcement: Two smooth copper-coated steel wires (2 mm diameter)

Sawing: Reduce length to 80 mm, keep the crack in the middle

Uncracked References: Outer parts (70 mm) sawn off

**For Corrosion Monitoring**

Reinforcement: One smooth steel bar (5.6 mm diameter)

Sawing: Reduce length to 50 mm, keep the crack in the middle

Uncracked References: Sawn to same dimensions as cracked samples

**Number of samples**

**For Ingress of Aggressive Agents**

10 uncracked, 10 with 100 µm cracks, 10 with 300 µm cracks

**For Corrosion Monitoring**

3 uncracked, 4 with 100 µm cracks, 4 with 300 µm cracks

**Inducing Cracks**

Method: Three-point bending at 28 days controlled with LVDT

Equipment: Walter-bai testing machine (15 kN capacity)

Target crack widths: 100 µm and 300 µm

**Healing regime**

**Healed Sample Preparation**

Duration: 3 months cyclic wet-dry (4 days wet/3 days dry)

**Unhealed Sample Preparation**

Storage: Standard laboratory condition (20°C, 60% RH) for the equivalent time

**Exposure conditions**

Solution Composition: According to ASTM D1141-98, prepared with demineralized water

Duration: one year

**For Ingress of Aggressive Agents**

Completely submerged in artificial seawater

**For Corrosion Monitoring**

On spacers, seawater level 5 ± 3 mm above bottom of samples

Seawater renewed every two weeks.

**Fig. 2.** Overview of the experimental program.

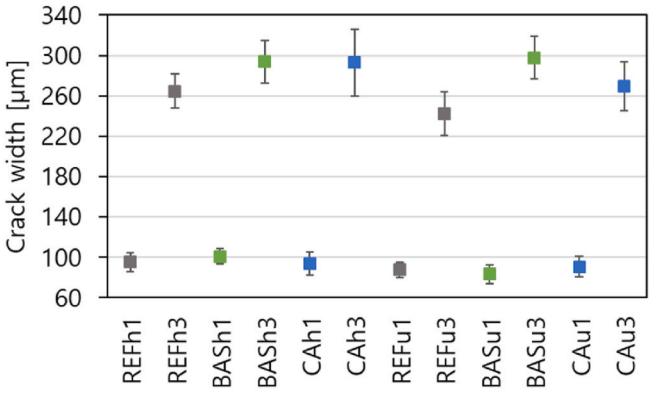


**Fig. 3.** Initial crack widths of different series.

low variability, reaching values near 100 µm, while larger cracks exhibited higher variability, ranging on average from 250 to 300 µm.

Fig. 4 is divided based on the specific timeframes where the self-healing efficiency (SE) for all the series was verified by microscopic image analysis. In this case, the SE estimation considered the initial crack width specific to each series. Overall, it is evident that series with initial crack widths of 100 µm generally exhibited higher SE compared to those with 300 µm widths. Notably, the healed series achieved the highest SE values for the 300 µm cracks, with BASh3 reaching 97% of SE compared to 88% for BASu3. In the case of CA, CAh3 reached a SE of 93%, whereas CAu3 showed a lower SE of 79%. However, for series with 100 µm crack widths, the SE values for unhealed and healed series were similar. The REF series exhibited the most significant crack closure after

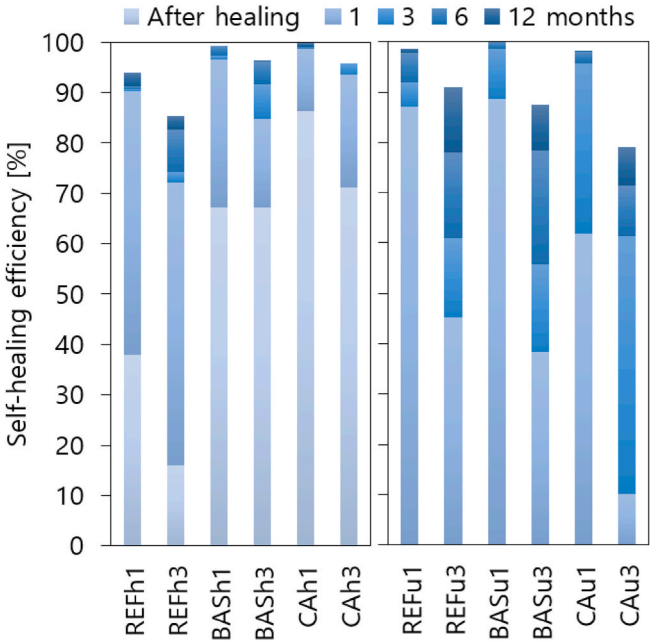


**Fig. 4.** Self-healing efficiency related to the initial crack width for all the series considered in the marine environment healed (h) and unhealed (u) samples until 12 months.

one month in seawater, surpassing BAS and CA. This can be attributed to a stronger chemical interaction with seawater, leading to the formation of a brucite or aragonite layer that contributed to visible crack closure (Alexander et al., 2013). This chemical interaction is likely attributed to the increased availability of $Ca(OH)_2$ in the REF matrix, which might be associated with its higher permeability. A similar behavior was observed for BASu, with a more evident crack closure observed after one month in seawater. Series with BAS and CA, which underwent the healing regime, displayed more pronounced crack closure after the healing process but less closure upon submerging the samples in artificial seawater.

Fig. 5 presents the relationship between crack width and self-healing efficiency by microscopic image analysis. The x-axis represents the initial crack width, while the y-axis shows the self-healing efficiency after 12 months of submersion in a simulated marine environment (seawater). The data points indicate that self-healing efficiency tends to be higher for smaller crack widths and decreases as the crack width increases. REF samples generally show lower self-healing efficiency compared to CA and BAS samples. Among the healed samples, the BASh series consistently achieves the highest self-healing efficiency, followed by the CAh series. The REFh samples exhibit the lowest self-healing efficiency among the healed samples. Unhealed samples (REFu, BASu, CAu) demonstrate significantly lower self-healing efficiencies across all crack widths compared to their healed equivalents, highlighting the efficiency of allowing specimens to heal before subjecting them to marine conditions.

### 3.2. Chloride penetration

Chloride penetration was assessed through two methods: the color change boundary method, through spraying silver nitrate, and the chemical analysis method via titration to determine chloride content. Fig. 6 illustrates chloride ingress through the color change boundary for the uncracked samples. In this analysis, BAS and CA were examined at four different ages (1, 3, 6, and 12 months). Evidently, the unhealed series displayed significantly higher chloride ingress compared to the series subjected to the healing regime. For instance, REFh managed to reduce chloride ingress by 86% when compared to the REFu series after 12 months exposure. Similar trends were observed for the BAS and CA healing agents, which achieved reductions of 82% and 85% in chloride

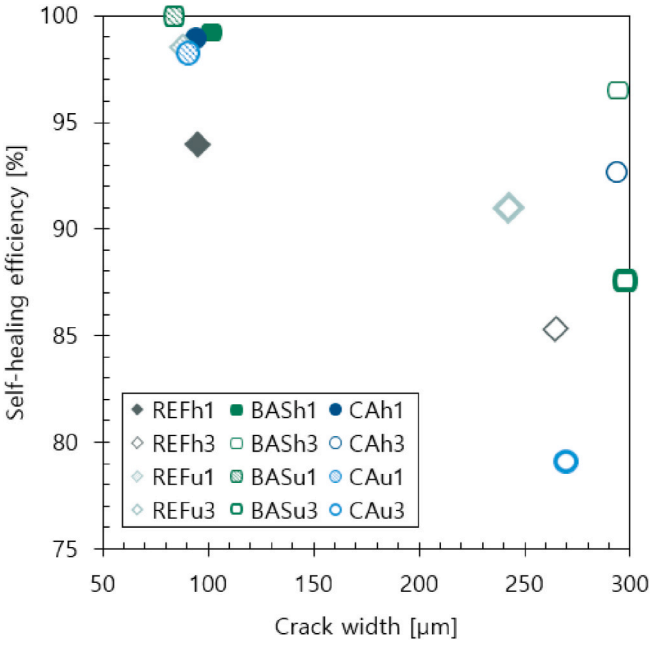


**Fig. 5.** Relationship between initial crack width and self-healing efficiency at 12 months of exposure.

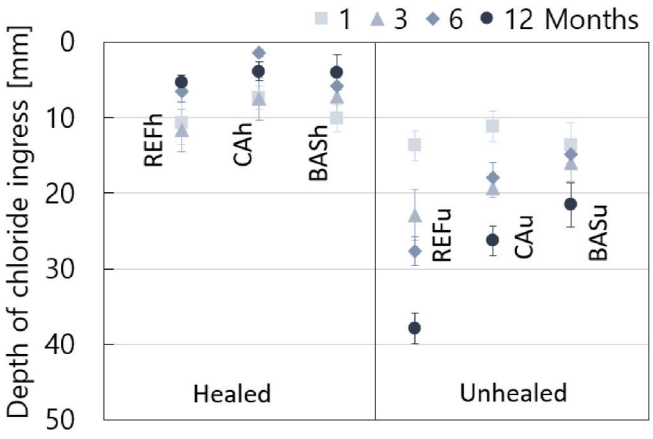


**Fig. 6.** Chloride ingress for the uncracked samples subjected to the marine environment. The error bars represent the standard deviation (n = 3).

ingress, respectively, in the healed series compared to the unhealed series. Notably, both healing agents (BAS and CA) outperformed their respective reference series. This difference is more evident for the unhealed series. For the healed series, the time in contact with water contributed to densification of the matrix by improving the cement hydration process, aiding to lower the permeability of the concrete. In this case, all the series, including the reference concrete (REFh), benefited from the healing regime due to the autogenous healing expected in the cementitious matrix (Hearn, 1998). The healing products densified the pore structure upon contact with seawater. This was achieved through the formation of healing products within the pores, leading to reduced permeability (Palin et al., 2017; Rossi et al., 2022; Oliveira et al., 2022; Cappellesso et al., 2022). While no clear differences were observed in the first month, the improvements in relation to REFu became increasingly evident after the third month, and particularly pronounced after one year.

To better evaluate the performance of each healing agent, it is crucial to analyze chloride ingress through cracks in the samples. Fig. 7 focuses on the healed and unhealed series of BAS and CA, comparing them to the REF series with an initial crack width of 100 µm. The healed samples demonstrated a reduction in chloride ingress compared to the unhealed samples. For instance, in the healed series, CAh1 (Fig. 7 (c)) managed to achieve 32% reduction in chloride ingress compared to REFh1 after 12 months exposure to a marine environment. In a study by Xue (2022a), the behavior of concrete with CA exposed to seawater in wet-dry cycles was investigated. The findings indicated that the formation of brucite within the cracks, because of the interaction with seawater, effectively reduced chloride ingress into those cracks. On the other hand, the BASh1 series (Fig. 7 (b)) exhibited an interesting behavior, with higher chloride ingress until the first 3 months of exposure, which then significantly decreased and approached levels similar to uncracked samples after 6 months, maintaining this behavior after one year of exposure. This peculiar behavior was primarily observed in the healed series. The complexity of artificial seawater, including its salt compositions, may have influenced the chemical interactions, potentially affecting the visually observed color change boundary. However, if seawater interaction was the sole reason, one would expect a similar behavior in the unhealed samples, which was not the case. This suggests that, in addition to the salt composition, bacterial activity encouraged by the healing regime may have played a significant role. The bacteria-based healing agent produces $CaCO_3$ as a healing product, and an excess of $CO_3^{2-}$ ions could trigger a false positive result with the silver nitrate indicator (Pontes et al., 2021). Specifically, silver ions ($Ag^+$) can react with $CO_3^{2-}$ to form $Ag_2CO_3$ (silver carbonate), resulting in a whitish color change.

Another factor that may have contributed to the observed differences is the greater crack depth in the BAS series, resulting from the testing

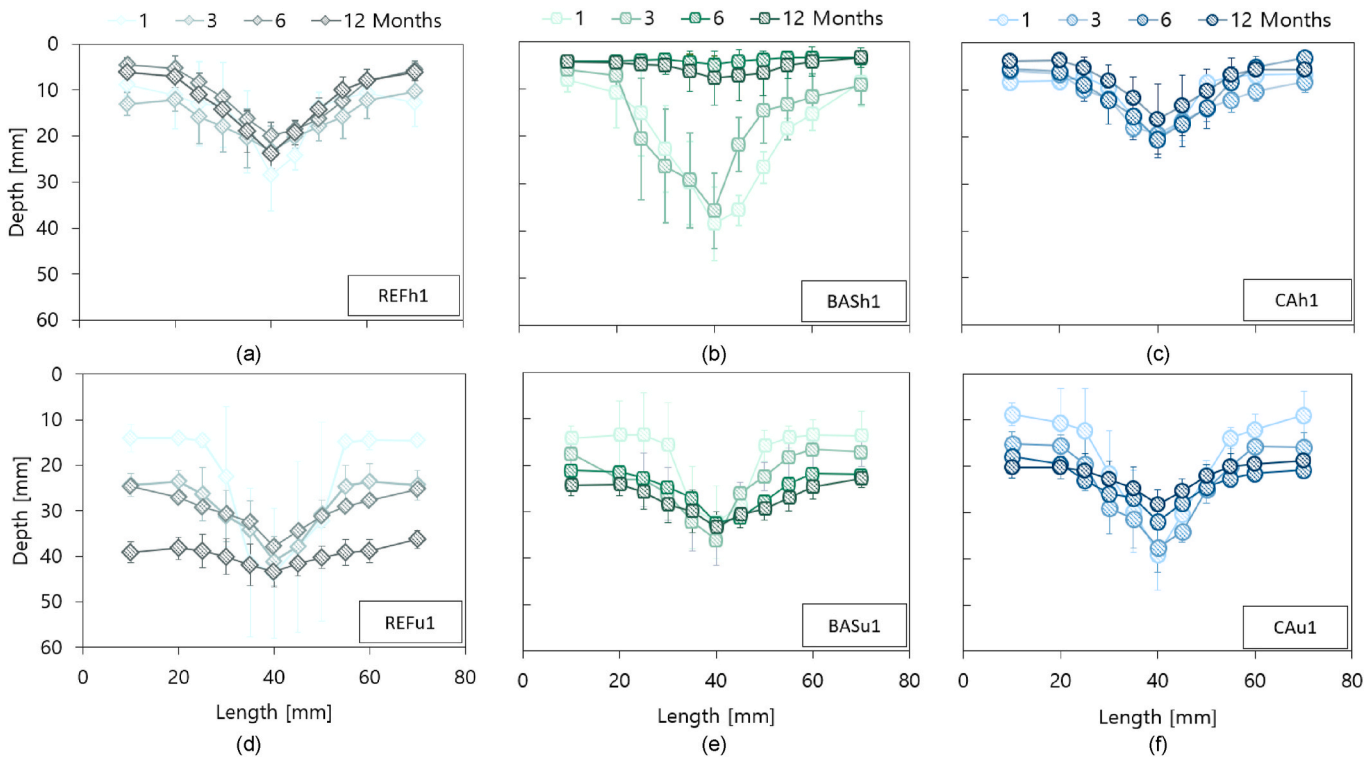


**Fig. 7.** Evolution of the chloride ingress for the series with crack width of 100 μm subjected to the marine environment (a) REFh1, (b) BASh1, (c) CAh1, (d) REFu1, (e) BASu1, and (f) CAu1. The error bars represent the standard deviation (n = 3).

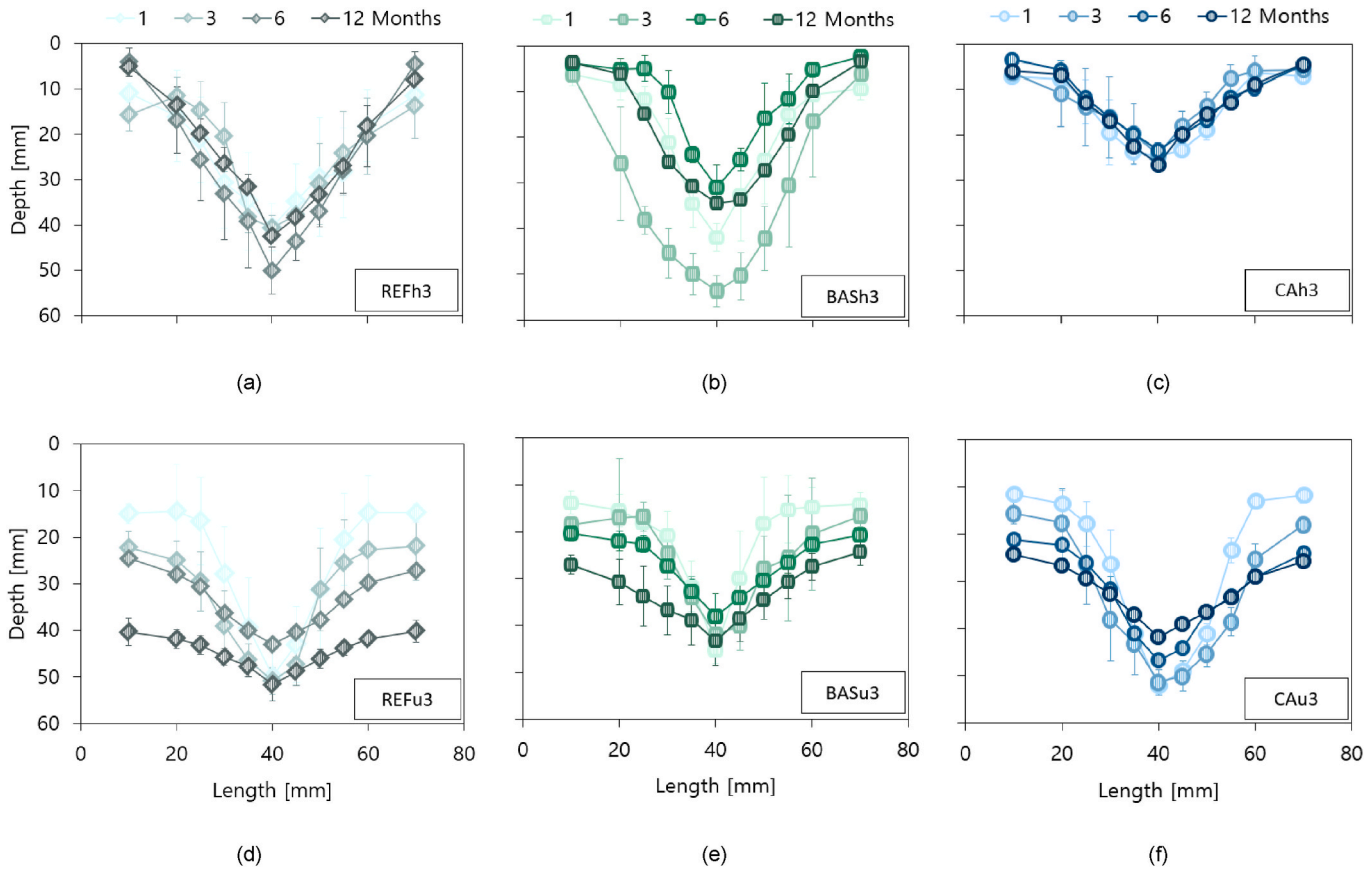


**Fig. 8.** Evolution of the chloride ingress for the series with crack width of 300 μm subjected to the marine environment (a) REFh3, (b) BASh3, (c) CAh3, (d) REFu3, (e) BASu3, and (f) CAu3. The error bars represent the standard deviation (n = 3).

method involving prisms cracked through a three-point bending test. Furthermore, in addition to bacterial activity, it is important to note that the BAS healing agent consists of up to 80% PLA (Green-Basilisk, 2018). PLA is a polar polymer with functional groups in its structure that can interact with ions (Constant-Mandiola et al., 2021). When PLA is exposed to an ionic environment, such as a solution containing salts or electrolytes, it can undergo hydrolysis and degradation due to interactions between ions and polymer chains. This degradation process results in the breakdown of PLA into water and carbon dioxide (Feng et al., 2021). The presence of carbon dioxide could contribute to the previously mentioned false positive results. The specific ions present in the environment, as well as their concentrations, can influence the rate and extent of PLA degradation. For instance, the presence of alkaline or alkaline earth metal ions like sodium, potassium, calcium, or magnesium ions can accelerate hydrolysis and degradation reactions. Additionally, the pH of the solution plays a role in PLA degradation in an ionic environment. Higher pH values, indicating an alkaline or basic environment, can increase the rate of hydrolysis and thus accelerate PLA degradation (Tsuji and Nakahara, 2002). It is worth noting that the pH of the solutions was carefully controlled over time and maintained within the range of 7.8–8.5. Nevertheless, despite these factors, BASh1 still achieved an impressive 68% reduction in chloride ingress compared to the REF1 series after 12 months in a marine environment.

Turning to the unhealed series, CAu1 (Fig. 7(f)) managed to reduce chloride ingress by 35% compared to REFu1 after 12 months. In contrast, BASu1 (Fig. 7(e)) resulted in a reduction of 23% in chloride ingress compared to REFu1. The differences in chloride ingress progression observed across all series, in healed and unhealed conditions, can be attributed to variations in crack characteristics, including width, depth, and tortuosity. Additionally, expansive reaction products like brucite, ettringite, and calcite may initially fill cracks and pores, serving as a barrier against further chloride ingress. However, over a longer term the sulfate and magnesium ion in chloride solution can lead to the decalcification of C–S–H compounds resulting in an increase in overall porosity, contributing to further degradation (Ramezanianpour et al., 2021).

Fig. 8 displays the results for series with larger initial crack widths. Like previous observations, the BASh3 series exhibited higher chloride ingress until the third month. The explanation for this behavior is similar as was described before. Nonetheless, despite this initial trend, BASh3 managed to achieve an 19% reduction in chloride ingress compared to REFh3 over the course of 12 months. On the other hand, the CAh3 series displayed a consistent behavior from the beginning of the exposure period, maintaining its performance until the 12-month mark, ultimately reducing chloride ingress by 38% compared to REFh3. In contrast, the unhealed series naturally exhibited higher chloride ingress due to their reduced contact with water. After 12 months, CAu3 demonstrated a 19% reduction in chloride ingress compared to REFu3, while BASu3 achieved a 16% reduction.

To estimate the chloride content, chemical titration analyses were conducted. The total chloride content relative to the binder for both uncracked REF, BAS, and CA series was verified, both in healed and unhealed conditions after three months of exposure to a marine environment. Figure S3 (Supplementary material) presents the graphics related to those series analysed. The healed series exhibited consistent behavior with minimal variations, maintaining the total chloride content below 0.5 wt% of the binder. Conversely, in the case of unhealed samples, the chloride content is significantly higher, reaching values between 2.5 and 3.0 wt% of the binder. BASu and CAu demonstrated higher diffusion coefficients (D) of $1.31x10^{-11}$ $m^2/s$ and $1.12x10^{-11}$ $m^2/s$, respectively, compared to REFu with a value of $7.11x10^{-12}$ $m^2/s$. Nevertheless, all three series demonstrated a comparable behavior, characterized by an equivalent total chloride concentration. In a chloride environment, CA has previously shown promising results in reducing chloride ingress (Cappellesso et al., 2022; Roig-Flores et al., 2015, 2016; Azarsa et al., 2019). Another study has also demonstrated evidence of chloride reduction when using a bacteria-based healing agent (Rossi et al., 2022; Tambunan et al., 2019). However, the effectiveness of bacteria-based healing agents can vary based on factors such as the type of bacteria used and the resulting porosity (Munyao et al., 2020). Rossi et al. (2022) observed the formation of a $CaCO_3$ layer on the surface, contributing to chloride ingress reduction and a lower pore volume when using this healing agent. Nevertheless, it is important to note that there are no previous results for concrete with these agents in a marine environment. Therefore, the reasons for chloride ingress may differ. The combination of salts, particularly sulfate and chloride salts, can influence the aggressiveness. Studies have shown that exposure to magnesium sulfate and sodium chloride combinations can lead to enhanced chloride ingress due to possible cracks caused by sulfate attack (De Weerdt et al., 2019). However, in marine concrete with lower sulfate concentrations, as found in seawater (around 30 mmol/l), the impact of sulfates on chloride ingress is generally limited. Studies conducted on marine-exposed concretes in Norway and Denmark have shown that, in these conditions, there is typically only an enrichment of sulfur near the surface of the concrete, with no or limited signs of damage (De Weerdt et al., 2019). Chemical interactions, such as sulfate reducing chloride binding capacity (Maes, 2015; Hirao et al., 2005), may also play a role. The blocking mechanism may involve multiple factors, including chemical interactions with artificial seawater. In addition, the formation of brucite and aragonite crystals, typical in marine environments (Alexander et al., 2013), can contribute to crack closure and act as a barrier against ingress.

After three months exposure, chloride ingress from the crack wall onwards was evaluated for cracked concrete at two depths, specifically at 15 mm and 40 mm depth. Fig. 9 presents the total chloride profiles for cracks with a width of 100 μm. As previously reported, the healed series (Fig. 9(a) and (c)) exhibited superior behavior compared to the unhealed series (Fig. 9(b) and (d)). The estimation of the diffusion coefficient (D) considered the diffusion mechanism from the crack wall onwards. In the healed series, chloride ingress at a depth of 40 mm was negligible, with values like the initial chloride levels measured in the concrete matrix. This suggests that narrow cracks were capable of healing completely, preventing chloride ingress at this depth. At a depth of 15 mm, the series containing BASh1 and CAh1 healing agents achieved lower chloride content and correspondingly lower D values, $2.22x10^{-12}$ $m^2/s$ and $5.21x10^{-12}$ $m^2/s$, respectively, versus $9.67x10^{-12}$ $m^2/s$ for REFh1. In contrast, in the case of unhealed series, chloride ingress could not be prevented at 40 mm depth. Among these unhealed series, CAu1 exhibited the lowest D value of $1.85x10^{-12}$ $m^2/s$ compared to BASu1 with a D value of $8.33x10^{-12}$ $m^2/s$ at 40 mm depth. At 15 mm depth, the unhealed series showed similar D values for REFu1 and BASu1, with values of $1.31x10^{-11}$ $m^2/s$ and $1.37x10^{-11}$ $m^2/s$, respectively. However, in this case, CAu1 had the highest D value of $3.24x10^{-11}$ $m^2/s$. It is worth noting that at 15 mm depth, the influence of chloride ingress from the top surface may also play a role, as ingress can occur from both directions, (top surface and crack wall). For this reason, the study conducted at a depth of 40 mm provides more robust conclusions about the performance of the healing agents.

In the case of larger cracks, there is a notable increase in chloride content, particularly for the unhealed series (Fig. 10(b) and (d)). However, like for the narrow cracks, the healed series with 300 μm wide cracks showed insignificant chloride ingress at a depth of 40 mm ((Fig. 10(c)). There was only a small increase in chloride content near the crack wall. For this reason, it was not possible to fit the Fick's law model to predict the D value for these series. At a depth of 15 mm ((Fig. 10(a)), BASh3 once again exhibited the lowest D value when compared to CAh3 and REFh3, with CAh3 having the highest diffusion coefficient. In the unhealed specimens, chloride ingress at 15 mm depth followed a similar trend across all the series (Fig. 10(b)), possibly due to the influence of chloride diffusion from the top surface. At a depth of 40 mm (Fig. 10(d)), BASu3 displayed higher chloride content, while CAu3 exhibited a behavior like that of REFu3.

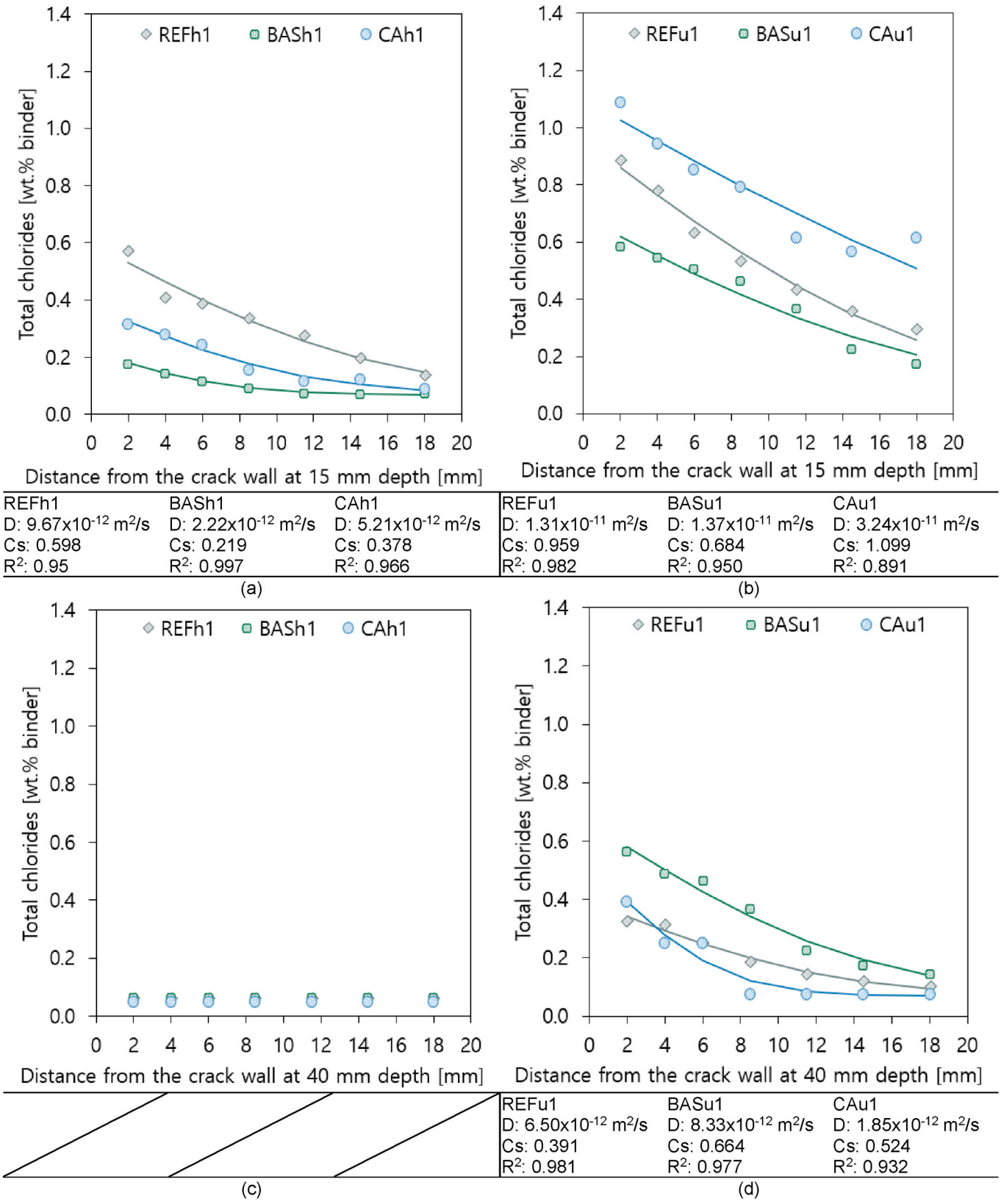


| REFh1 | BASh1 | CAh1 |
|---|---|---|
| D: $9.67\times10^{-12}$ m²/s | D: $2.22\times10^{-12}$ m²/s | D: $5.21\times10^{-12}$ m²/s |
| Cs: 0.598 | Cs: 0.219 | Cs: 0.378 |
| $R^2$: 0.95 | $R^2$: 0.997 | $R^2$: 0.966 |

(a)

| REFu1 | BASu1 | CAu1 |
|---|---|---|
| D: $1.31\times10^{-11}$ m²/s | D: $1.37\times10^{-11}$ m²/s | D: $3.24\times10^{-11}$ m²/s |
| Cs: 0.959 | Cs: 0.684 | Cs: 1.099 |
| $R^2$: 0.982 | $R^2$: 0.950 | $R^2$: 0.891 |

(b)

(c)

| REFu1 | BASu1 | CAu1 |
|---|---|---|
| D: $6.50\times10^{-12}$ m²/s | D: $8.33\times10^{-12}$ m²/s | D: $1.85\times10^{-12}$ m²/s |
| Cs: 0.391 | Cs: 0.664 | Cs: 0.524 |
| $R^2$: 0.981 | $R^2$: 0.977 | $R^2$: 0.932 |

(d)

**Fig. 9.** Chloride profile for the 100 μm cracked REF, BAS and CA series subjected to marine environmental condition at 3 months (a) healed series at 15 mm depth (c) at 40 mm depth, (b) unhealed samples at 15 mm depth and (d) at 40 mm depth.

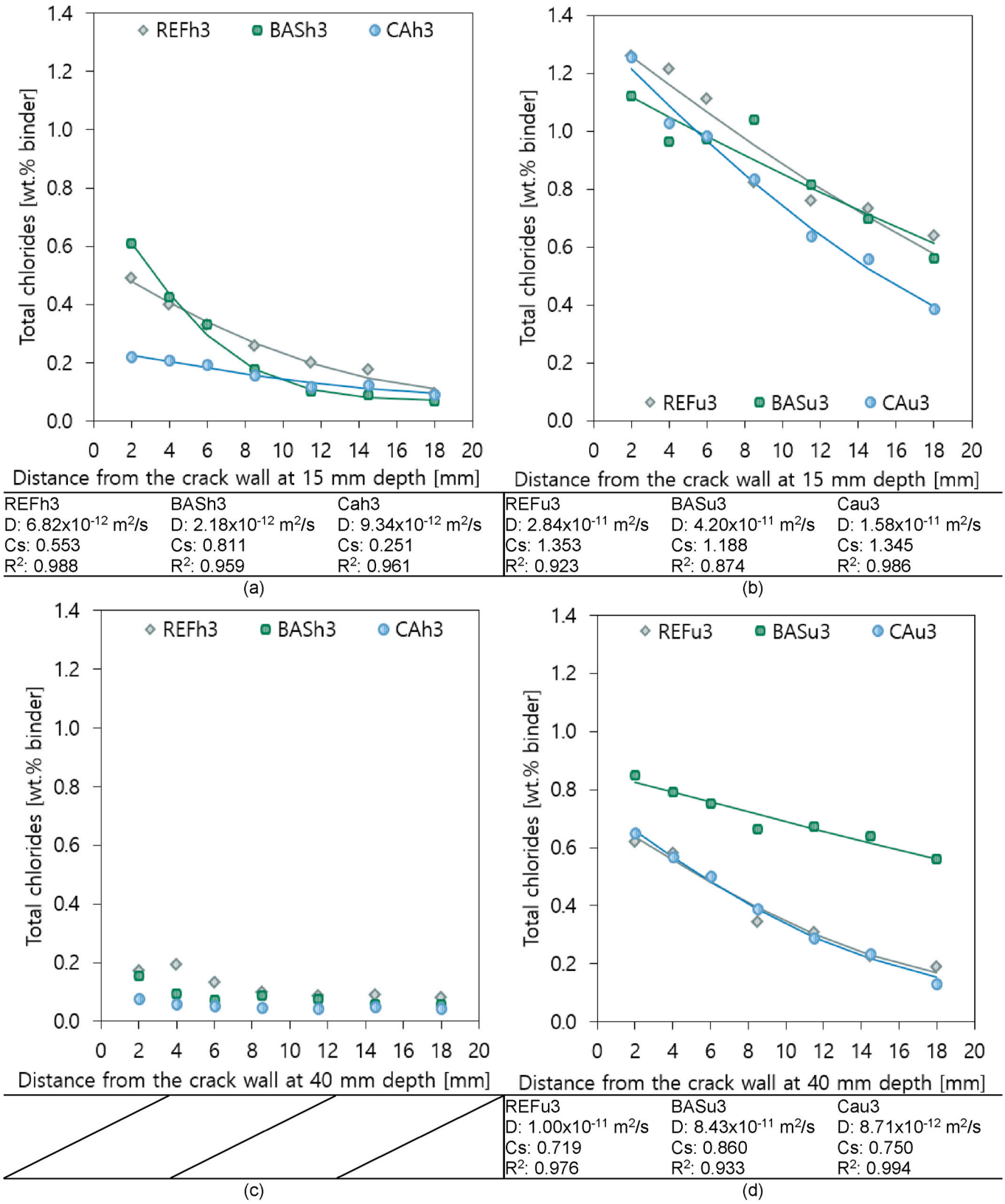


**Fig. 10.** Chloride profile for the 300 μm cracked REF, BAS and CA series subjected to marine environment at 3 months (a) healed series at 15 mm depth (c) at 40 mm depth, (b) unhealed samples at 15 mm depth and (d) at 40 mm depth.

After 12 months exposing the samples to the marine environment, a new chemical analysis was conducted, specifically on the uncracked samples (Fig. 11). During this process, the quantification of the free chloride content aimed to verify the binding capacity of the concrete series containing healing agents. Free chloride content in concrete refers to the concentration of chloride ions in the pore solution that remain unbound chemically. In contrast, total chloride content includes both free chloride ions and those chemically bound within the cementitious

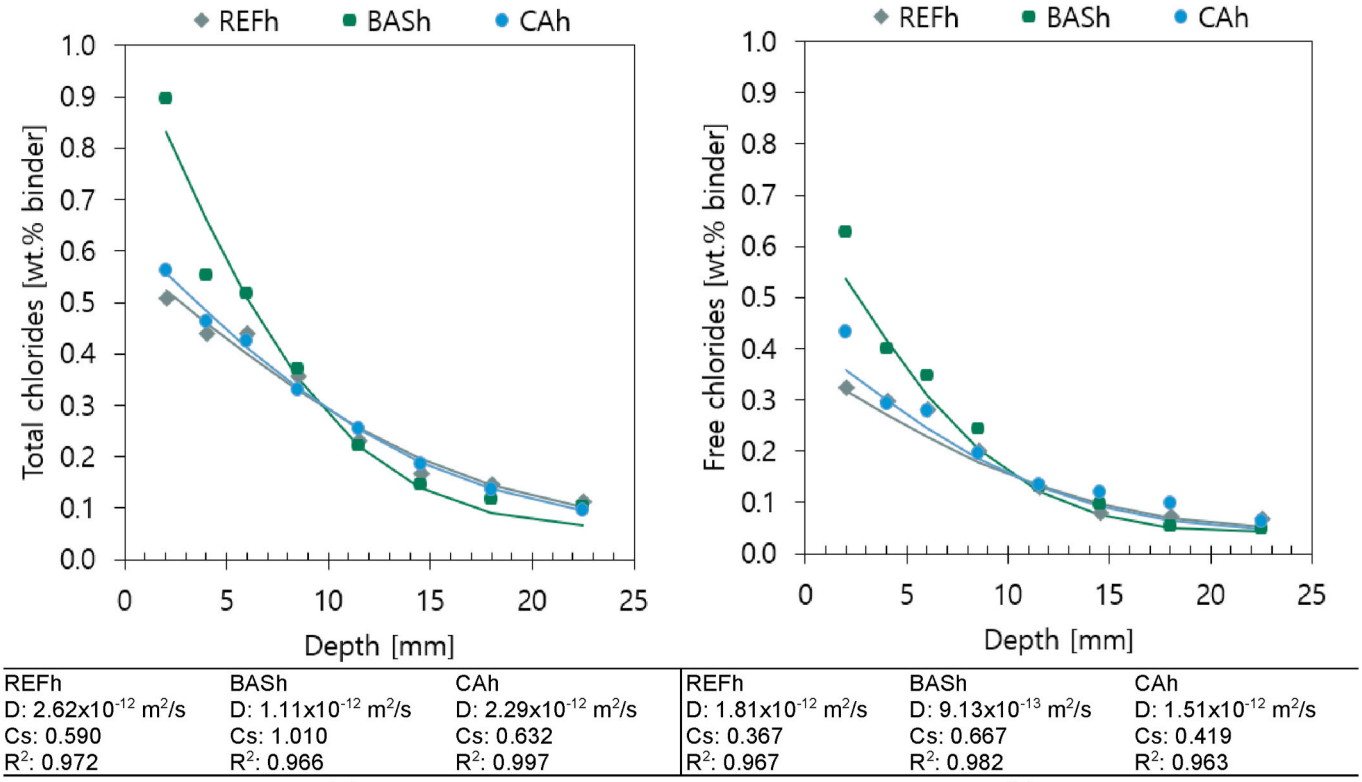


| REFh | BASh | CAh |
|---|---|---|
| D: 2.62x10$^{-12}$ m$^2$/s | D: 1.11x10$^{-12}$ m$^2$/s | D: 2.29x10$^{-12}$ m$^2$/s |
| Cs: 0.590 | Cs: 1.010 | Cs: 0.632 |
| $R^2$: 0.972 | $R^2$: 0.966 | $R^2$: 0.997 |

(a)

| REFh | BASh | CAh |
|---|---|---|
| D: 1.81x10$^{-12}$ m$^2$/s | D: 9.13x10$^{-13}$ m$^2$/s | D: 1.51x10$^{-12}$ m$^2$/s |
| Cs: 0.367 | Cs: 0.667 | Cs: 0.419 |
| $R^2$: 0.967 | $R^2$: 0.982 | $R^2$: 0.963 |

(b)

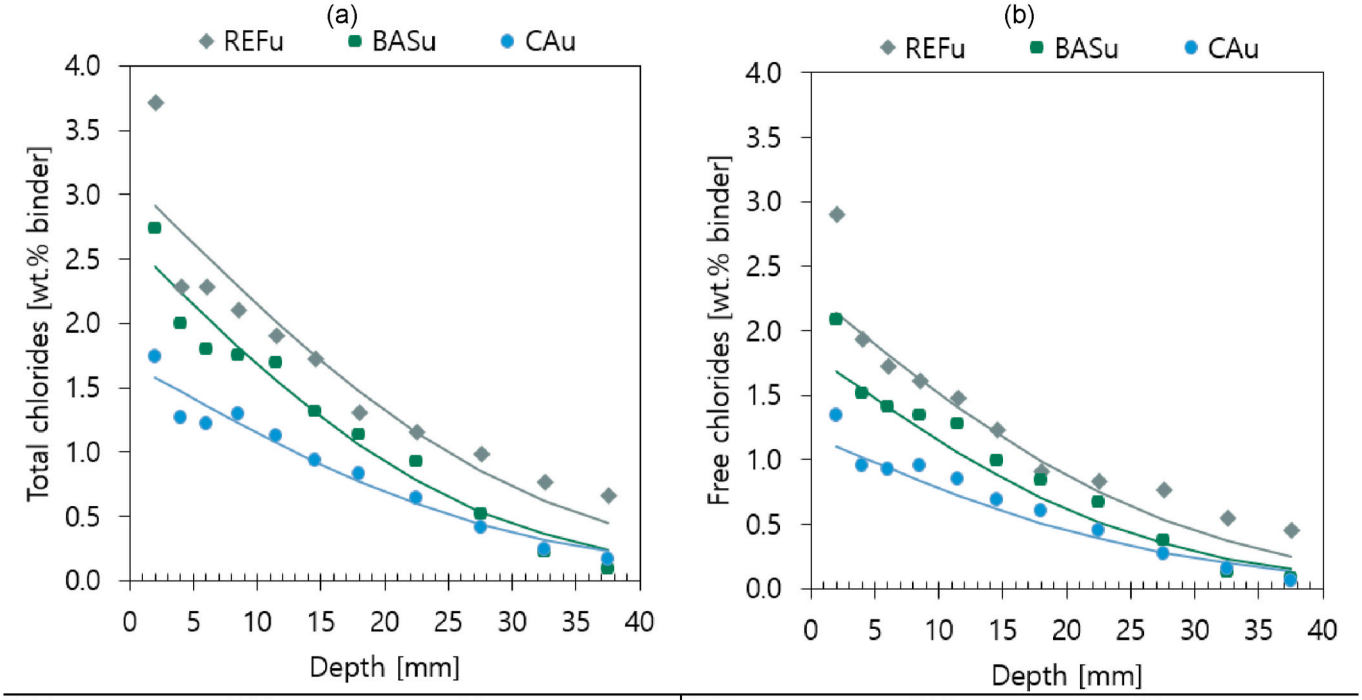


| REFu | BASu | CAu |
|---|---|---|
| D: 9.52x10$^{-12}$ m$^2$/s | D: 6.85x10$^{-12}$ m$^2$/s | D: 8.44x10$^{-12}$ m$^2$/s |
| Cs: 3.112 | Cs: 2.635 | Cs: 1.694 |
| $R^2$: 0.868 | $R^2$: 0.953 | $R^2$: 0.955 |

(c)

| REFu | BASu | CAu |
|---|---|---|
| D: 7.97x10$^{-12}$ m$^2$/s | D: 6.45x10$^{-12}$ m$^2$/s | D: 7.57x10$^{-12}$ m$^2$/s |
| Cs: 2.295 | Cs: 1.825 | Cs: 1.186 |
| $R^2$: 0.885 | $R^2$: 0.958 | $R^2$: 0.958 |

(d)

**Fig. 11.** Chloride profile for the uncracked REF, BAS and CA series subjected to marine environmental condition at 12 months (a) total chloride and (b) free chloride profile for healed series, and (c) total chloride and (d) free chloride profile for unhealed series.

matrix. Both data sets exhibit a consistent trend, indicating uniform chloride binding across various depths. However, it is important to note that the estimation of free chloride relies on the model proposed by Yuan (2009). Variations in hydration products and differences in curing time and healing time can introduce variability. This estimation offers valuable insights into how healing agents may interact with chloride binding and their potential role in reducing corrosion initiation in real-world conditions. In the healed series, the D value for total chloride content was lower for BASh than for CAh and REFh, measuring $1.11x10^{-12}$ $m^2/s$. The D value for free chloride content exhibited the same tendency, showing the lowest value of $9.13x10^{-13}$ $m^2/s$. It is worth mentioning that the chloride ingress can be influenced by other factors. For example, concrete carbonation can lead to the formation of calcium carbonate, which may reduce concrete permeability and slow down chloride ingress. However, carbonation can also compromise the stability of Friedel's salt, leading to increased free chloride content and potentially accelerated chloride ingress (Backus and McPolin, 2016). On the other hand, an elevated concentration of chloride ions in the outer layers may indicate a stronger binding effect, limiting the penetration of chloride ions into deeper layers that will be further discussed in Fig. 12. The carbonates formed due to the activity of BAS may have contributed to influence the binding capacity and porosity of the matrix in the outer layers, resulting in higher chloride content up to a depth of 10 mm. Notably, there was a decrease to lower values, likely due to porosity blocking or the binding capacity. In the case of CAh, its behavior closely mirrored that of REFh, with a gradual reduction in the D value for CAh. The behavior of the unhealed samples concerning both total and free chloride content also followed a similar trend, indicating comparable binding capacity among the series.

To determine the bound chloride levels within each tested series, one can subtract the free chlorides from the total chloride content. To better differentiate between the series, the data was normalized using the minimum-maximum normalization method. This resulted in a common scale for comparison across different types of concrete. Fig. 12 presents a comparison between the BAS and CA series under both unhealed and healed conditions. From Fig. 12(a), the healed series showed no significant difference in bound chloride when introducing the healing agents. Fig. 12(b) shows that this difference is more pronounced for the unhealed samples. A slight reduction in the binding capacity was noticed when introducing the healing agents compared to the REFu series. The significance of understanding cementitious materials' capacity to bind chlorides becomes evident in managing the initiation of chloride-induced corrosion in reinforced concrete structures (Mangat and Ojedokun, 2020). This importance stems from the fact that only free chloride ions have the potential to initiate the corrosion process. Delving into the composition of hydrated phases reveals its crucial role in determining chloride binding capacity. The presence of chloride-binding compounds, such as C–S–H and monocarbonate, plays a pivotal role in reducing the availability of free chloride ions within the concrete matrix (Costa and Appleton, 1999). Additionally, $C_3A$ and $C_4AF$ phases have been identified as being responsible for chemically binding chloride ions. Interestingly, an increase in sulfate content in cement tends to diminish the chloride binding capacity due to the stronger affinity of sulfates for $C_3A$ compared to chlorides. The physical binding, on the other hand, depends on the quantity of hydration products, especially the C–S–H content within the concrete (Sumranwanich and Tangtermsirikul, 2004).

### 3.3. Mass change

Fig. 13 presents the evolution of mass changes over 12 months for BAS and CA concrete in comparison to REF, considering both the series subjected to the weekly wet-dry cycles for three months before exposure, named healed (h), and the series subjected directly to a marine environment, named unhealed (u). Notably, the healed series, owing to the reduced permeability resulting from the healing regime, exhibited minimal mass changes over time, with no significant differences when considering the scale of mass change. However, when examining the behavior closely, the CA series followed a similar trend to REFh, while BASh initially experienced mass loss, which peaked at three months before gradually experiencing a mass increase. In contrast, the unhealed samples (Fig. 13(b)) displayed an opposite trend, with mass gain observed over time in all series. This can be attributed to the formation of reaction products. Among these, CAu demonstrated the least variation less than 1.0%, aligning with expectations as this healing agent is designed to contribute to waterproofing the concrete matrix by obstructing pores and capillaries with healing products (Oliveira et al., 2022). CA also altered the pore structure of the matrix, increasing micropores and potentially interrupting pore connectivity (Cappellesso, 2024). Furthermore, the interaction with seawater influenced the behavior of concrete containing healing agents. BASu exhibited a mass change like REFu until the seventh month, after which it showed a more significant change in the twelfth month, 2.9% and 2.7%, respectively. Unlike isolated sulfate attack, seawater interactions involve a complex interplay of salts, which can delay concrete degradation due to the presence of several ions (De Weerdt et al., 2019). In summary, these

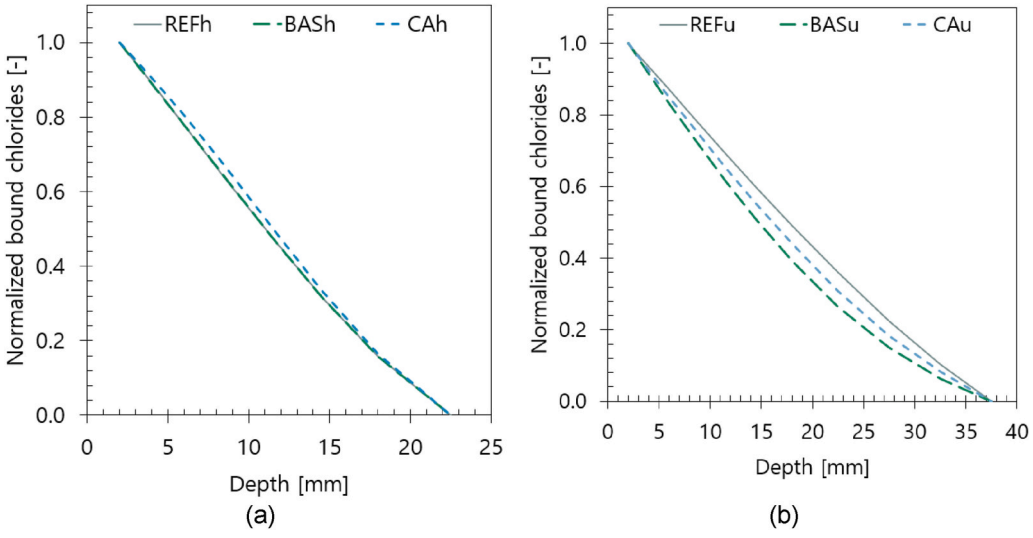


**Fig. 12.** Bound chloride profile for the uncracked REF, BAS and CA series subjected to marine environmental condition at 12 months (a) healed and (b) unhealed series.

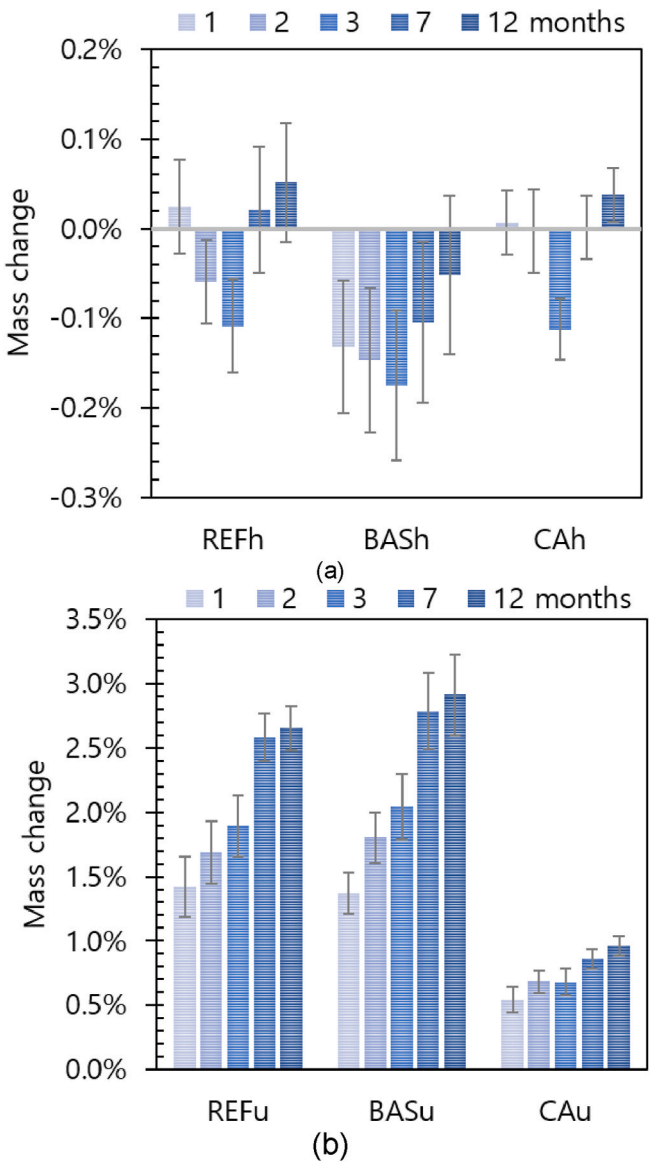


**Fig. 13.** Changes in mass for REF, BAS and CA concrete under marine environment: (a) the series subjected to the weekly wet-dry cycles for three months before exposure, named healed and (b) the series subjected directly to a marine environment, named unhealed. (n = 10).

observations highlight the intricate dynamics of concrete exposed to artificial seawater in the presence of healing agents, shedding light on both healing-related effects and the influence of the marine environment on concrete mass changes.

### 3.4. Microstructural analysis after exposure to marine environment

The microstructural analysis played a crucial role in elucidating the products formed in the BAS and CA series after a year of exposure. Thin sections of the cracked samples were examined by XPL. Interestingly, in the series subjected to a healing regime, there was no clear presence of a brucite or aragonite layer on the surface. In contrast, the series exposed directly to the marine environment without a healing regime showed the presence of a protective layer on the surface (Fig. 14). This protective layer also played a role in sealing the cracks in the case of the samples with cracks, similar as observed in literature (Ramezanianpour et al., 2021; Mohammed et al., 2003). It is worth noting that when analyzing the products formed within the cracks, findings are consistent with findings reported in existing literature (Danner et al., 2019). In the uncracked samples, the analysis revealed a different crystal formation according to the series. In XPL images, brucite usually presents as colorless or very pale in color, characterized by its low birefringence (δ). Ettringite, on the other hand, appears predominantly grey (δ = 0.008), while in carbonate crystals display a bright yellow color (δ = 0.150) being defined as aragonite due to the contact with marine solutions reported in literature. Observing Fig. 14, it becomes apparent that REFu displayed a combination of brucite and ettringite beneath a clearly defined aragonite layer. Likewise, in the case of CAu, an aragonite layer was present, although less prominently, and beneath it, brucite was the dominant mineral, with no discernible ettringite formation. In contrast, BASu exhibited a brucite layer with no apparent evidence of aragonite or ettringite formation.

In the unhealed cracked samples, a similar analysis was performed, but with a focus on the crystals formed at the crack mouth and deeper within the crack (Figure S4 - Supplementary material). In all three series, the crystal formations on the top surface and within the first few millimeters deeper into the crack exhibited the same pattern as reported in Fig. 14. This layer effectively closed the crack mouth, with the protective layer primarily composed of brucite in the case of BASu3 and CAu3, and with more evidence of ettringite and aragonite in the case of REFu3. When observing the crystals formed a few millimeters below this protective layer, ettringite emerged as the main crystal formation across all three series. The crystals of secondary ettringite exhibited a grey to dark color, consistent with previous reports, and displayed specific needle or fibrous features. When examining the entire crack, REFu3 was limited to forming ettringite close to the surface and below the protective layer, with only a few occurrences of ettringite formation in the crack wall. In

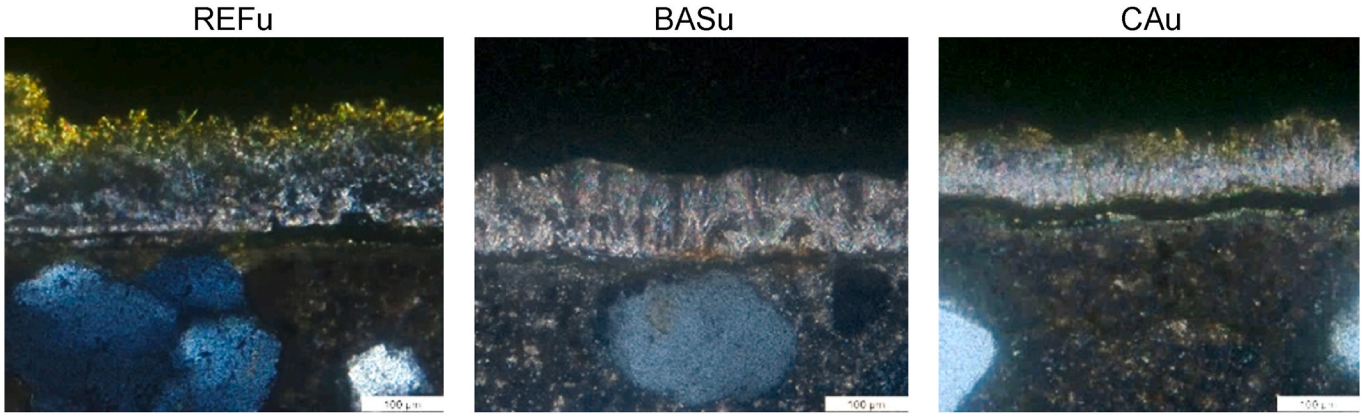


**Fig. 14.** Evidence of a protective layer formed by brucite, ettringite and aragonite at the concrete surfaces by XPL images of the uncracked REFu, BASu and CAu series after 12 months in marine environment. The scale bars represent 100 μm.

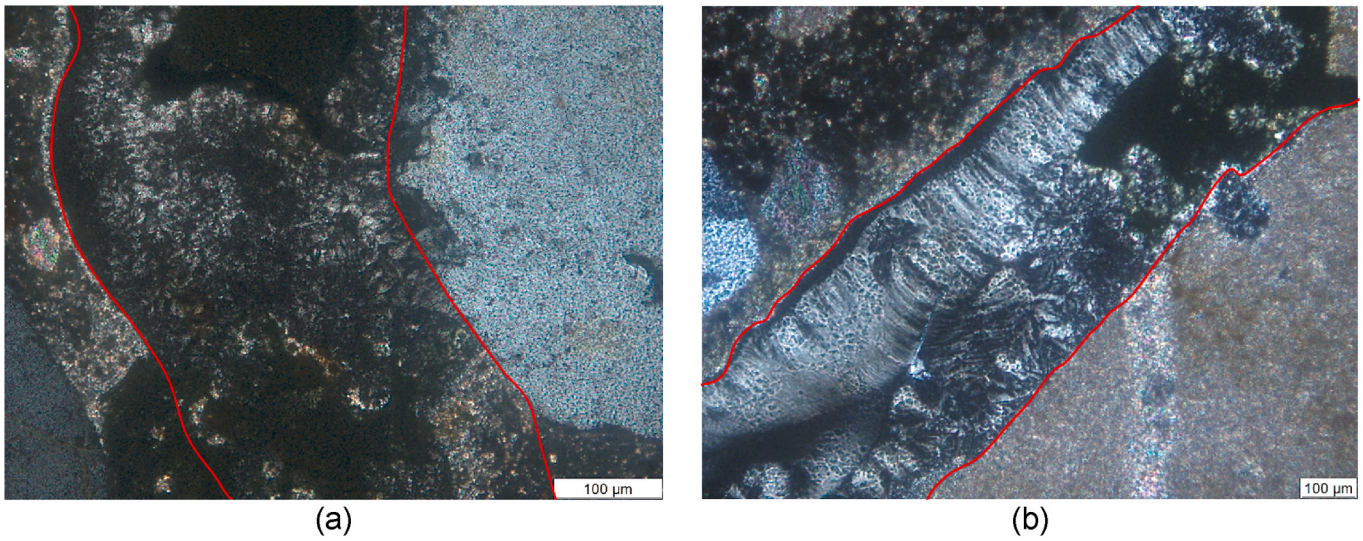


**Fig. 15.** Evidence of ettringite formation by XPL images deeper in the crack of (a) BASu3 and (b) CAu3 after 12 months in marine environment. The scale bars represent 100 µm.

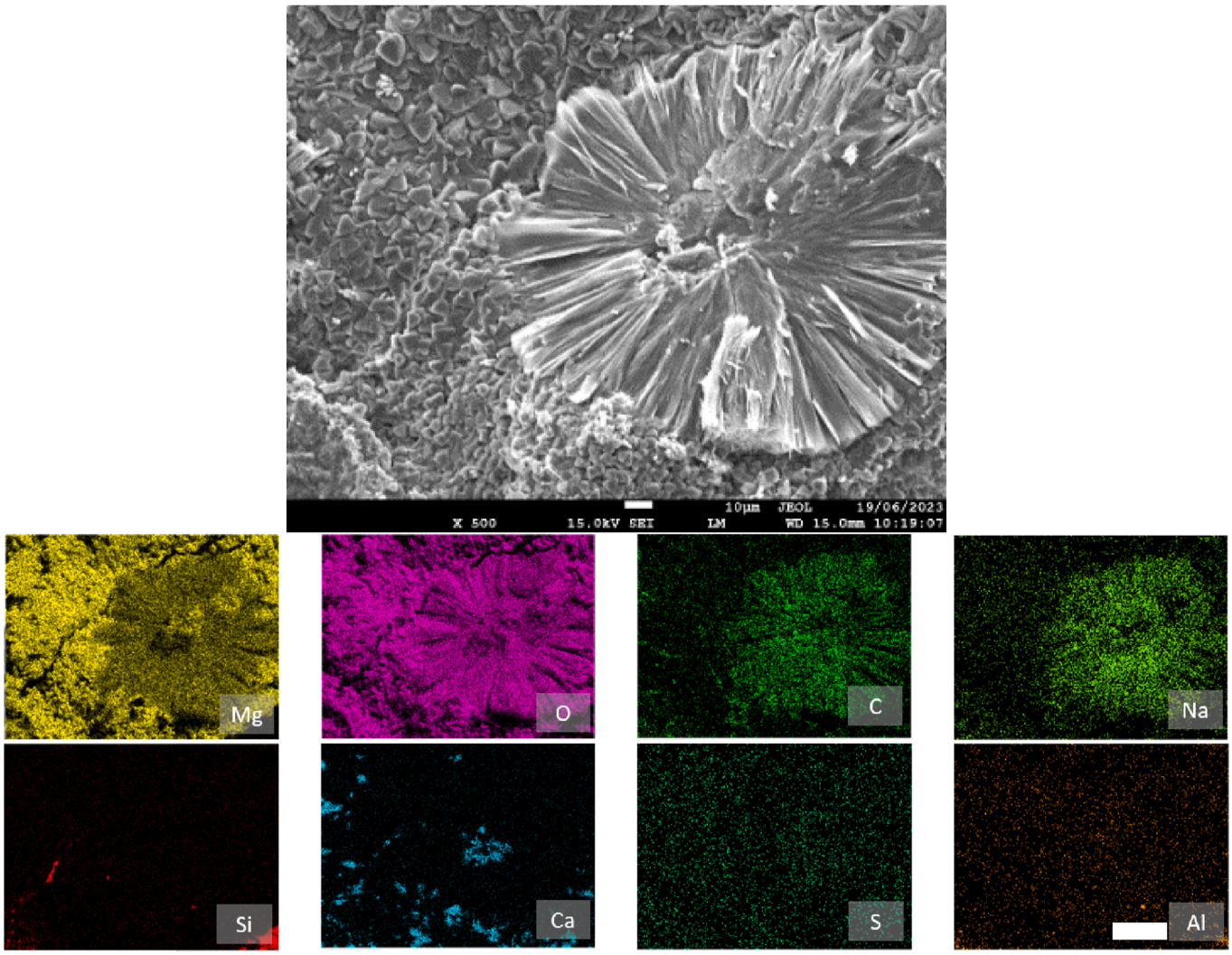


**Fig. 16.** EDX mapping analysis on the crack wall of the BASh3 samples after 12 months under marine environment with brucite and sodium carbonate crystals. The scale bars in the SE images represent 10 µm, and in the mapping images 50 µm.

contrast, BASu3 and CAu3 demonstrated more significant blockage of the crack filled with ettringite. Fig. 15 depicts the fibrous secondary ettringite formed within the cracks of BASu3 and CAu3, with the edges of the cracks highlighted by red lines.

In addition, the examination of the inner portions of the cracks involved a combined approach of SEM and EDX analysis to identify the crystalline structures present. In the case of REFh3 (Figure S5 - Supplementary material), the analysis revealed the presence of aragonite, a finding supported by both the chemical composition and crystal morphology. Aragonite, a less stable phase of calcite that forms under specific exposure conditions (Han et al., 2005), possesses a chemical composition primarily consisting of Ca, O, and C. This composition is supported by the EDX developed in the REFh3 sample, revealing that it comprises 42% Ca, 40% O, and 16% C. The needle-shaped morphology observed further corroborates the indication of this unstable calcite phase (Chen and Xiang, 2009). The formation of aragonite is a commonly observed phenomenon in concrete exposed to seawater (Alexander et al., 2013). It is anticipated that beneath the aragonite layer, a layer of brucite exists and was already evidenced in the previous section. They act as a barrier against further damage, which is in line with findings from Mohammed et al. (2003), who reported the presence of ettringite, calcite, and brucite inside cracks when subjected to a marine environment. Furthermore, the research conducted by Danner et al. (2019) corroborated these observations. Their work indicated the formation of calcite in the outer part of the crack, followed by a brucite layer, with ettringite primarily observed in the deeper regions of the crack.

In contrast, BASh3 exhibited primarily the formation of brucite ($Mg(OH)_2$) (Figure S6 - Supplementary material) and the potential presence of crystals, such as sodium carbonate (Fig. 16 and Figure S7 - Supplementary material). These crystalline precipitates were primarily observed in the BAS series after exposure. This phenomenon is likely attributed to the hydrolysis of PLA (which is 50–80 wt% of the bacterial pellets) in combination with the activation of bacteria, which may release $CO_2$. This release of $CO_2$ could contribute to an increased carbon content within the concrete matrix, serving as a source for the reactions that lead to the formation of sodium carbonate. In contrast, Palin et al. (2015), who studied a similar healing agent, only documented the formation of brucite in the inner regions of the cracks, which was associated with the presence of magnesium ions in the seawater, but they did not notice any interaction with the sodium. Furthermore, Khan et al. (2021a) conducted a study that verified the presence of aragonite, alongside brucite formation, in mortar containing spores of *Sporosarcina halophila* bacteria, calcium lactate, and expanded perlite aggregate as the carrier, after 90 days of exposure. It is worth noting that the shape of the crystals formed in concrete can be influenced by various factors, including the environmental conditions and the specific bacterial species used. Bacteria, such as *Bacillus subtilis* and *Bacillus megaterium*, have been found to play a significant role in the formation of crystals in concrete. These bacteria can produce exopolysaccharides and amino acids that influence the mineralogy and morphology of calcium carbonate crystals (Zhou et al., 2014; Braissant et al., 2003). The addition of nutrients, such as calcium sources, can further affect the shape of the crystals formed (Nasser et al., 2022).

In the CAh3 series after exposure, mainly ettringite was identified ($6CaO.Al_2O_3.3SO_3.32H_2O$) and brucite was found on the crack walls (Figure S8 and S.9 - Supplementary material). This aligns with findings by Xue (2022b), who confirmed the presence of brucite within cracks in concrete containing CA exposed to seawater. Additionally, He et al. (2020), observed the formation of calcium carbonate alongside brucite as healing product within cracks when a CA was used.

In the unhealed series, specifically in the case of REFu3, the predominant crystals found were aragonite, accompanied with brucite within the crack walls. Notably, a distinct layer of aragonite encased a layer of brucite, a phenomenon commonly observed in seawater due to elevated levels of dissolved $CO_2$ (Skalny et al., 1999). This layered

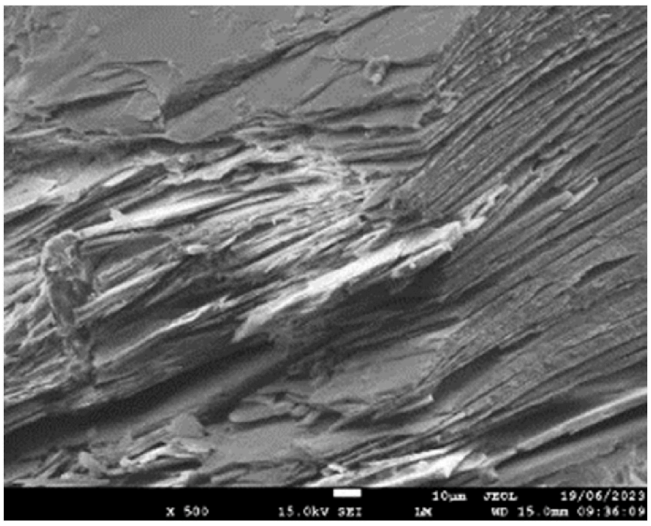


**Fig. 17.** SEM image on the crack wall of the BASu3 sample after 12 months in marine environment with laminar calcium carbonate formation. The scale bars in the SE images represent 10 µm.

structure serves as an additional barrier mechanism within the material. In the case of BASu3, a distinct pattern of crystal formation emerged (Fig. 17), characterized by layers composed primarily of oxygen (48.4 wt%) and calcium (44.0 wt%). These layers also contained trace amounts of carbon (5.9 wt%), silica (0.6 wt%), and a smaller quantity of magnesium (0.5 wt%). This composition strongly suggests the predominant formation of calcium carbonate. Notably, the laminar shape of these crystals was particularly evident in the BASu series. Additionally, the analysis revealed the presence of ettringite and brucite, clustered around these laminar calcium carbonate crystals (Figure S10 - Supplementary material).

In the CAu3 series, the analysis indicated the presence of brucite (Figure S11 – Supplementary material). Furthermore, both ettringite and calcium carbonate formations were identified. Interestingly, this crystal formation closely resembled what was observed in the healed series.

### 3.5. Corrosion monitoring in the self-healing concrete

The corrosion potential versus time has been plotted for each series, starting from the moment samples were brought in contact with seawater, all the way through 360 days of monitoring. In Fig. 18 the uncracked samples are presented with the grey area denoting the threshold defined in Section 2.5. This area represents an intermediate probability of corrosion initiation. Above this threshold (above −126 mV), the probability is low, while below it (below −276 mV), the probability for corrosion initiation is high. It is worth noting that for some samples, the corrosion potential falls within the range indicating an intermediate probability of corrosion in the initial period. This occurrence is linked to the preconditioning of each series. During the healing regime, the healed series were in contact with water, but the edges of the rebars were protected with a sealant, as outlined in the methodology. This ensured that the uncracked healed series began with initial potential values indicating a low risk of corrosion initiation. However, the unhealed series were stored with the rebars exposed to a climate-controlled room (20 °C, 60% RH). Over time, the humidity in the room appears to have caused some corrosion at the rebar edges while the samples awaited the same aging period to enter the marine environment, along with the healed samples. Prior to the samples being exposed to the marine environment, the edges of the rebars were sanded, and they were protected in accordance with the sample preparation. This corrosion is evident from the more negative initial values observed.

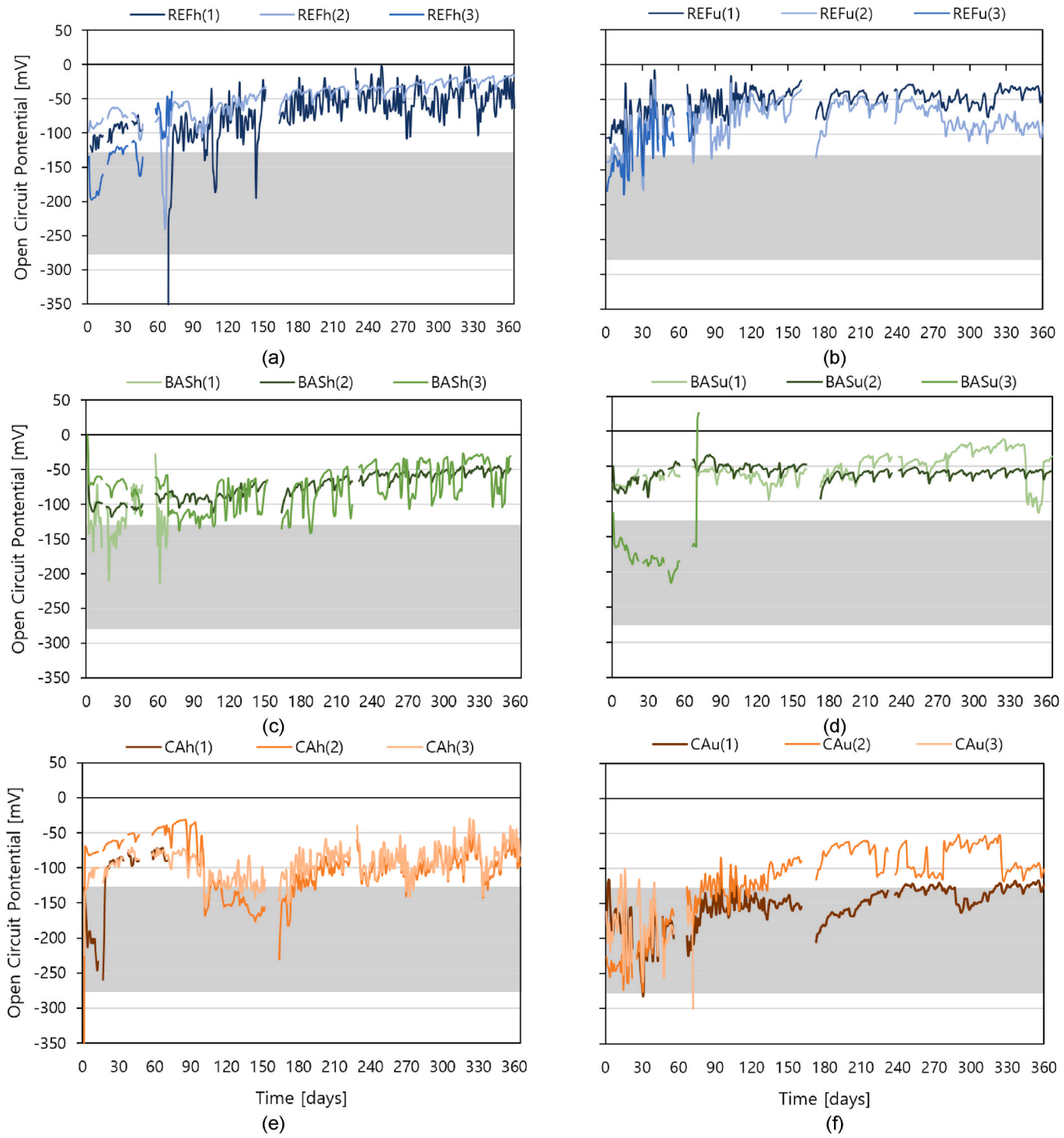


**Fig. 18.** Evolution of the Open Circuit Potential individual values measured against a saturated calomel electrode in the reinforcement of different uncracked series, healed and unhealed, tested in marine environment (a) REFh, (b) REFu, (c) BASh, (d) BASu, (e) CAh and (f) CAu. Considering three samples per series named from 1 to 3.

During the experiment, the rebars seemed to reactivate the passivation stage, with the values returning to a low probability of corrosion. Protecting the rebar edges at that stage may have limited corrosion by blocking access to oxygen and water. This could lead to repassivation, restoring structural integrity by stabilizing the pore solution and promoting realkalization of the outer zone. Additionally, upon removal of the rebars from the samples, corrosion was only evident in the REF series. Consequently, the initiation period was not clearly observable for any of the uncracked series. It is possible that for a more extended exposure period, corrosion initiation might become evident later. As an interesting reference, Du et al. (2020) conducted experiments mimicking marine exposure using cracked concrete beams and a concrete cover of 25 mm. They found that it took 700 days to induce corrosion in cracks with a width of 100 μm, whereas for cracks of 300 μm, this time was reduced to 460 days. Uncracked samples were not included in their experiment, but it is likely that they would require even longer exposure periods. Note that in the current study the used concrete cover was 20 mm.

Figure S12 (Supplementary material) presents the results for the series with 100 μm wide cracks. Among these series, only REFu1 and CAh1 showed a corrosion potential in the low probability range for corrosion initiation. BASu1, on the other hand, had one sample indicating corrosion initiation after 22 days of exposure, signified by a drop in potential, but the other BASu1 samples were very similar to the CAh1 behavior. CAu1 samples started in the intermediate probability zone and reached values indicative of a high probability of corrosion around 12 days of exposure. Another CAu1 sample exhibited a similar drop in potential after 117 days of exposure. REFh1 showed corrosion initiation between 58 and 74 days for some samples, followed by a passivation period, and later, a continuous decrease in corrosion potential after 257 days. BASh1 demonstrated a similar pattern to REFh1, with corrosion initiation observed in two samples at 58 and 74 days. It is important to note that relying on only one method of measurement cannot provide a comprehensive understanding of corrosion propagation. Further discussion will elucidate these findings in next sections.

In the case of larger cracks (Figure S13 - Supplementary material), all series reached a high probability of corrosion, typically after 60–70 days. Larger cracks inherently carry a higher risk of corrosion. Kušter Marić et al. (Kušter Marić et al., 2020) found that cracks larger than 100 μm significantly reduce depassivation time, regardless of the cover thickness. Montes et al. (2004) observed that increasing crack widths from 250 μm to 500 μm exacerbates corrosion due to marine exposure. Otieno et al. (2016) noted that cover thickness can prevent corrosion in narrow cracks, but it has only a limited effect on wider cracks (400 μm and 700 μm). Lopez-Calvo et al. (2018) showed that corrosion potential increases with crack width in a simulated marine tidal condition. In the context of this thesis, the healing agents were unable to prevent corrosion in cracks measuring 300 μm. However, in the case of narrow cracks, specifically 100 μm wide, CAh demonstrated the capability to protect the reinforcement against corrosion.

### 3.6. *In-depth examination of reinforcement: visual, gravimetric, and chemical analysis*

The visual examination of rebars involved identifying corroded areas (Fig. 19). Among the uncracked samples, only the REF series displayed corrosion pits at the bottom part of the rebar, being the first location of contact with the solution, with more significant corrosion observed in the unhealed series. In contrast, samples with healing agents did not show any sign of corrosion at the reinforcement for the uncracked samples. The indication of corrosion in the uncracked samples was due to the presence of chloride ingress, which was confirmed by spraying silver nitrate on the samples after the 360-day exposure to the marine environment. For the narrow-cracked samples, only CAh1 effectively prevented corrosion of the reinforcement, while BASh1 failed to do so, showing heavy corrosion pits even within the narrow cracks. Of the healed specimens, the REFh series performed the worst in terms of visual damage caused to the rebars due to contact with the simulated seawater. When examining samples with larger cracks across all series, corrosion pits were typically observed, with the corrosion often being more severe in the crack areas. However, in some series, corrosion initiated at the edges or bottom of the rebar. This suggests that the healing products formed were unable to prevent chloride ingress leading to subsequent corrosion of the reinforcement and caused some flaws in the homogeneity of the concrete protecting the rebar. In the case of narrow cracks, only CAh1 proved effective in restricting chloride ingress and preventing corrosion of the reinforcement. In the unhealed cracked series, regardless of the crack size, corrosion pits were observed. As cracks serve as pathways for aggressive substances, it becomes evident that without the application of a healing regime, healing agents cannot prevent the corrosion of the reinforcement.

Fig. 20 illustrates the gravimetric analysis, quantifying the mass loss of the reinforcement for all the series under consideration. Notably, the uncracked samples exhibited less mass loss when compared to the cracked samples. Among the cracked samples, there is not a discernible trend of mass loss directly correlated with the crack width. However, it is more evident that the CAh series displayed lower mass loss compared to the other healed series. Conversely, both REFh and REFu exhibited the highest mass loss when compared to the concrete containing the healing agents. A statistical analysis was carried out to evaluate the impact of cracked concrete at 100 and 300 μm, pre-conditioning (healed vs unhealed) and three types of concrete (REF, BAS, and CA). The Test of Normality showed normality of the data with a level of significance of 5% and a $p$-value greater than 5% for all data groups, except for BAS 300 μm which had a $p$-value of 1.0%. ANOVA tests were performed to determine the equality of means with a significance level of 5%. For unhealed 100 μm ($p$-value = 40.2%) and 300 μm ($p$-value = 53.2%), and for healed 300 μm ($p$-value = 48.2%), equality of means was assumed. However, for healed 100 μm, ANOVA testing showed a difference in means with a significance level of 5% and a $p$-value of 0.9%. Based on a Tukey test with a significance level of 5%, REF was found to be significantly different from the others for healed 100 μm, with p-values of 0.9% and 4.0% for the differences between CA-REF and BAS-REF, respectively (no statistical difference for BAS-CA with a $p$-value of 41.7%).

The initial focus of the EDX analysis was on the surface of an

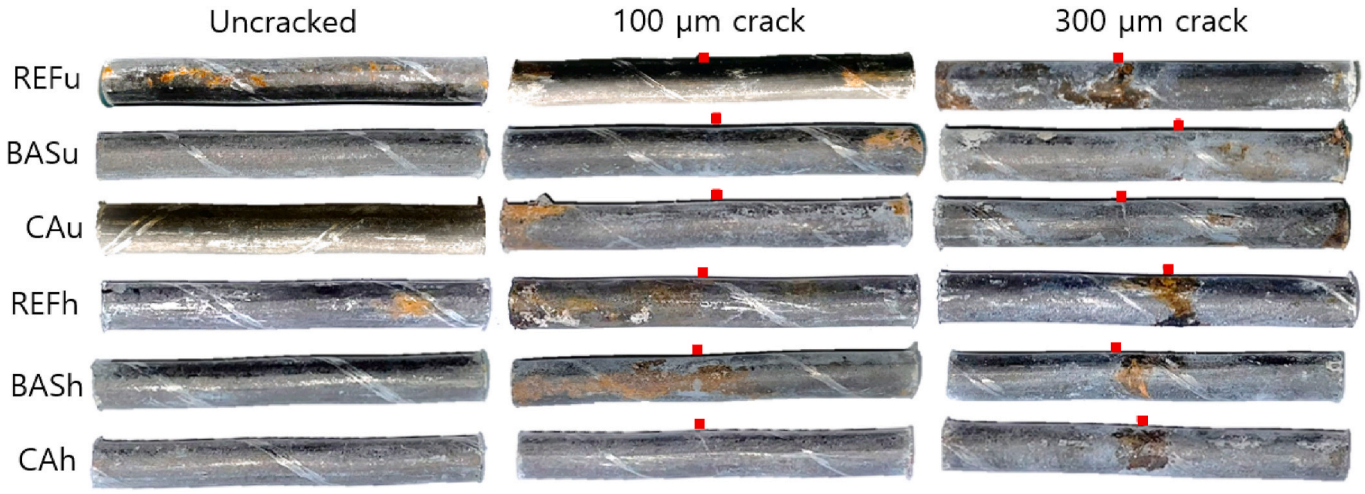


**Fig. 19.** Representative photographs of the series subjected to the corrosion experiment in marine environment. The red markers indicate where the crack intersected the rebar. (For interpretation of the references to color in this figure legend, the reader is referred to the Web version of this article.)

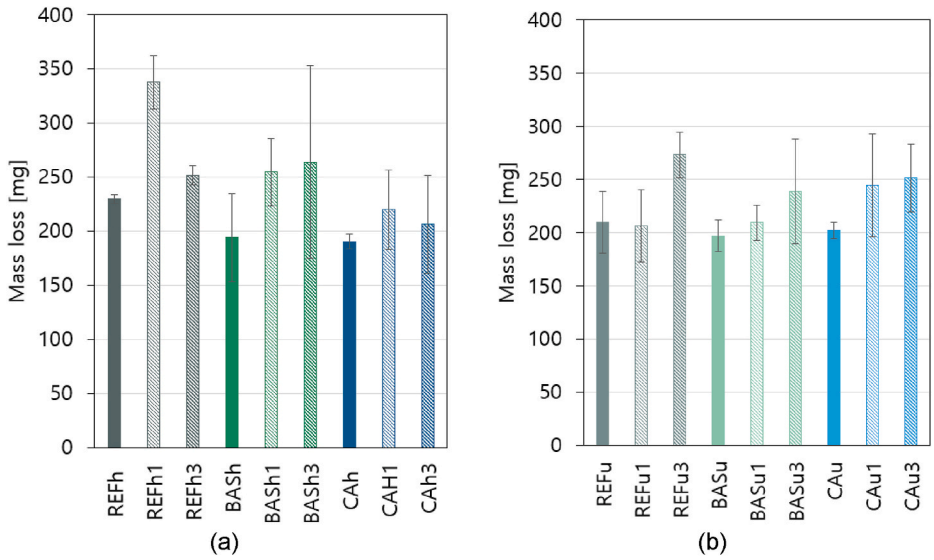


**Fig. 20.** Mass loss for the series subjected to the corrosion experiment (a) healed series and (b) unhealed series. The error bars represent the standard deviation (n = 2 for the uncracked series and n = 3 for the cracked series).

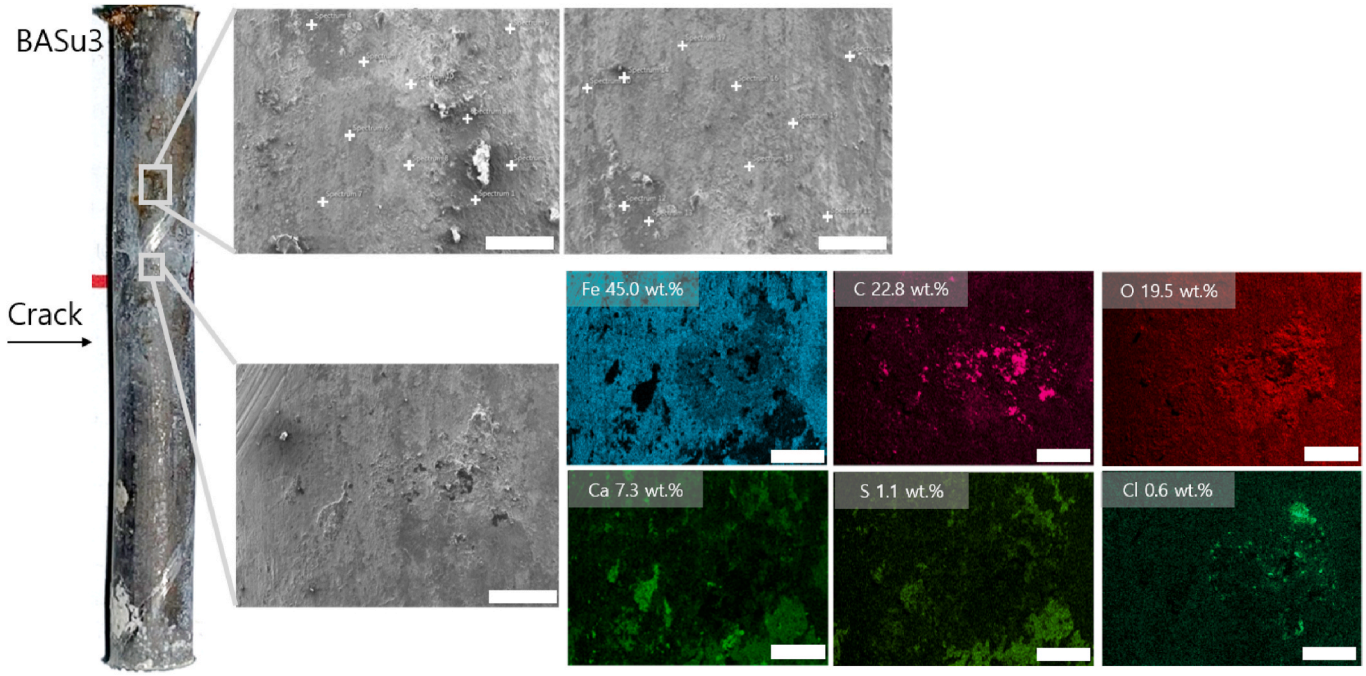


**Fig. 21.** Illustration of data collection via EDX point analyses in a corroded area, incorporating two locations with a minimum of 10 data points each, alongside EDX mapping in the crack region. The scale bars represent 500 μm.

unexposed steel rebar, aiming to determine its precise composition in terms of $Fe_xO_y$ and Fe (wt.%). Subsequently, the surface compositions of the exposed steel rebars were analysed, as exemplified in Fig. 21. For each series, a minimum of two spots, each containing ten EDX points, were examined to quantify the elements present in the corroded area. Reductions in the $Fe_xO_y$ content (wt.%) served as indicators to define the level of corrosion among rebars obtained from different batches. In the case of an unexposed rebar, its surface composition comprised 70.9% Fe, 10.4% O, and 14.1% C, which are primary elements in most steel alloys. The quantification of the corroded area for each concrete type is presented in Fig. 22. The unexposed rebar provides a baseline for comparison with the studied series. Importantly, as corrosion progressed, the Fe content on the corroded rebar's surface decreased. Concurrently, other metals present in the rebar alloy, such as copper, chromium, and aluminum, became detectable due to the degradation of the passive layer (Erşan et al., 2018). The EDX mapping in Fig. 21 serves as an illustrative example of how seawater can affect the rebar, revealing the presence of chloride and sulfur in the crack area, which contribute to the initiation of the corrosion process. In Fig. 22, the quantification reveals distinct trends among the different series. In the case of unhealed samples, REFu exhibits the most significant decrease in Fe content at 27.7%. In contrast, when healing agents are introduced, BASu and CAu experience minor reductions of 19.4% and 12.2%, respectively, compared to the unexposed rebar. However, for the healed series, a different pattern emerges. The impact on Fe content is more pronounced in the presence of the CAh healing agent, displaying a reduction of 22.3% compared to

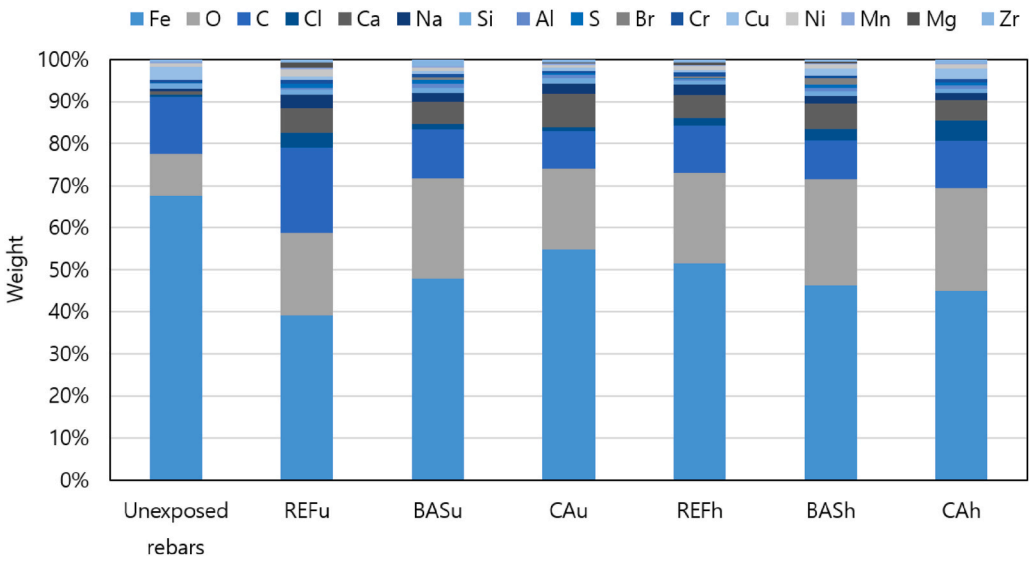


**Fig. 22.** Assessing the effects by EDX point analyses of 360 days of marine exposure on the passive oxide layer and surface composition of the rebars comparing the series studied with the unexposed rebar. Average of minimum 20 points.

the unexposed rebar. This is followed by BASh with a 19.8% decrease and REFh with a 15.2% decrease. These findings suggest that the healing regime employed in the series containing healing agents affects the depassivation layer of the reinforcement, leading to a decrease in Fe content. Additionally, the healed series exhibit an increase in the weight of oxygen (O). Specifically, BASh shows the highest increase at 17.6%, followed by CAh with a 16.3% increase and REFh with a 13.0% increase. On the other hand, the unhealed series generally experience lower increases in O content, except for BACu, which observes a substantial 15.3% increase compared to the unexposed rebar. Meanwhile, CAu has a 10.2% increase, and REFu has an 11.2% increase in O content.

## 4. Conclusions

A thorough assessment of two healing agents was conducted (a bacteria-based healing agent (BAS) and a crystalline admixture (CA)), with a primary focus on how they perform when used in concrete exposed to a marine environment. Concrete samples were immersed in artificial seawater in accordance with ASTM D1141-98 (2021). The results revealed that these healing agents can significantly reduce the chloride ingress rates. Consequently, they have the potential to enhance the overall resilience of concrete when exposed to the challenging marine environment.

After 12 months of exposure, the BAS improved the concrete matrix, reducing chloride ingress by 43% in uncracked, unhealed samples compared to the reference series without healing agent. The chloride ingress was reduced by 23% at the location of the crack in case of narrow cracks (100 μm) and by 16% in case of large cracks (300 μm). In healed samples chloride ingress was reduced by 68% at the location of the crack in case of narrow cracks, but for large cracks, this value decreased to 19%. The BAS series had the highest mass gain after 12 months of exposure for the unhealed uncracked series and the highest mass loss for the healed samples. In unhealed samples, a brucite layer sealed the crack mouth, and notable ettringite formation in the initial millimeters of the crack effectively blocked it. This phenomenon was less prominent in the healed samples. In the healed samples, evidence of sodium carbonate crystals was noticed on the crack walls by SEM analysis. In contrast, in the unhealed samples, distinct laminar crystals of calcium carbonate in combination with ettringite were found. The BAS could not avoid corrosion of the reinforcement in cracked concrete regardless of the crack width, being able to avoid corrosion only in uncracked samples.

In the CA series the concrete matrix was improved, resulting in a significant reduction of chloride ingress by 31% in uncracked and unhealed samples compared to the reference series after 12 months of exposure. At the same exposure time, chloride ingress was reduced in healed samples, showing a 32% decrease in narrow cracks and a 38% decrease in large cracks at the crack location. In unhealed narrow and wide cracks, chloride ingress was reduced by 35% and 19% respectively when compared to reference samples without healing agent. The CA series did not show any significant changes in mass over time. In unhealed samples, a layer of mainly brucite and less pronounced aragonite sealed the crack mouth, and ettringite formation was noticed in the initial millimeters and deeper in the crack. This phenomenon was not observed in the healed samples. SEM analysis revealed the presence of ettringite and brucite formation on the crack wall of the healed and unhealed samples. The CA healing agent effectively prevented reinforcement corrosion in uncracked samples and in samples with narrow healed cracks. However, in the unhealed series and in samples with large cracks, regardless of the healing regime, corrosion was evident.

In conclusion, the choice of a healing agent for marine environments demands careful consideration, depending on the specific application and crack conditions. The BAS and CA healing agent have been found to be effective in marine environments, as long as the concrete is uncracked or has narrow cracks. However, while BAS is unable to prevent corrosion, CA could prevent reinforcement corrosion in healed samples and samples with narrow cracks. Although there are challenges with certain healing agents, their overall contribution to enhancing concrete durability and reducing chloride ingress was significant. This highlights the importance of tailored solutions to address the unique demands of marine environments.

## CRediT authorship contribution statement

**Vanessa Giaretton Cappellesso:** Writing – original draft, Visualization, Methodology, Investigation, Formal analysis, Data curation, Conceptualization. **Tim Van Mullem:** Writing – review & editing, Validation. **Elke Gruyaert:** Writing – review & editing, Supervision, Resources, Methodology, Funding acquisition, Conceptualization. **Kim Van Tittelboom:** Writing – review & editing, Supervision, Methodology, Funding acquisition, Conceptualization. **Nele De Belie:** Writing – review & editing, Supervision, Resources, Funding acquisition, Conceptualization.

## Declaration of competing interest

The authors declare that they have no known competing financial interests or personal relationships that could have appeared to influence the work reported in this paper.

## Data availability

Data will be made available on request.

## Acknowledgements

This project has received funding from the European Union's Horizon 2020 research and innovation programme under the Marie Skłodowska-Curie grant agreement N° 860006.

The authors would like to thank Basilisk (The Netherlands) and TU Delft for providing the bacteria-based healing agent and Penetron Italia Srl, for providing the crystalline admixture agent.

## Appendix A. Supplementary data

Supplementary data to this article can be found online at https://doi.org/10.1016/j.dibe.2024.100486.

## References

Alexander, M., Bertron, A., De Belie, N., 2013. Performance of cement-based materials in aggressive aqueous environments. https://doi.org/10.1007/978-94-007-5413-3.
Almashakbeh, Y., Saleh, E., Al-Akhras, N.M., 2022. Evaluation of half-cell potential measurements for reinforced concrete corrosion. Coatings 12, 975. https://doi.org/10.3390/coatings12070975.
ASTM C876-15, 2016. Standard Test Method for Corrosion Potentials of Uncoated Reinforcing Steel in Concrete. West Conshohocken, PA, USA.
ASTM D1141 – 98, 2021. Standard Practice for Preparation of Substitute Ocean Water. ASTM International, West Conshohocken, PA.
Azarsa, P., Gupta, R., Biparva, A., 2019. Assessment of self-healing and durability parameters of concretes incorporating crystalline admixtures and Portland Limestone Cement. Cem. Concr. Compos. 99, 17–31. https://doi.org/10.1016/j.cemconcomp.2019.02.017.
Backus, J., McPolin, D., 2016. Effect of cyclic carbonation on chloride ingression in GGBS concrete. J. Mater. Civ. Eng. 28 https://doi.org/10.1061/(ASCE)MT.1943-5533.0001529.
Basilisk-Contracting, B.V., 2019. Basilisk - Material Safety Data Sheet. Concrete Healing Agent – PLA based (CHA-PLA), Delft,The Netherlands, p. 9. https://www.basiliskconcrete.com/wp-content/uploads/2019/12/20181019_HA_MSDS_Material-Safety-Data-Sheet.pdf.
Biczok, I., 1967. Concrete Corrosion Concrete Protection. Chemical Publishing Company Inc., NY.
Braissant, O., Cailleau, G., Dupraz, C., Verrecchia, E.P., 2003. Bacterially induced mineralization of calcium carbonate in terrestrial environments: the role of exopolysaccharides and amino acids. J. Sediment. Res. 73, 485–490. https://doi.org/10.1306/111302730485.
Cappellesso, V.G., 2024. Self-healing Concrete in Aggressive Environments. Ghent University and KU Leuven University.
Cappellesso, V.G., Petry, N. dos S., Longhi, M.A., Masuero, A.B., Dal Molin, D.C.C., 2022. Reduction of concrete permeability using admixtures or surface treatments. Journal of Building Pathology and Rehabilitation 7, 38. https://doi.org/10.1007/s41024-022-00176-z.
Cappellesso, V.G., di Summa, D., Pourhaji, P., Prabhu Kannikachalam, N., Dabral, K., Ferrara, L., Cruz Alonso, M., Camacho, E., Gruyaert, E., De Belie, N., 2023a. A review of the efficiency of self-healing concrete technologies for durable and sustainable concrete under realistic conditions. Int. Mater. Rev. 68, 556–603. https://doi.org/10.1080/09506608.2022.2145747.
Cappellesso, V., Van Mullem, T., Gruyaert, E., Van Tittelboom, K., De Belie, N., 2023b. Bacteria-based self-healing concrete exposed to frost salt scaling. Cem. Concr. Compos. 139, 105016 https://doi.org/10.1016/j.cemconcomp.2023.105016.
Chen, J., Xiang, L., 2009. Controllable synthesis of calcium carbonate polymorphs at different temperatures. Powder Technol. 189, 64–69. https://doi.org/10.1016/j.powtec.2008.06.004.
Constant-Mandiola, B., Aguilar-Bolados, H., Geshev, J., Quíjada, R., 2021. Study of the influence of magnetite nanoparticles supported on thermally reduced graphene oxide as filler on the mechanical and magnetic properties of polypropylene and polylactic acid nanocomposites. Polymers 13, 1635. https://doi.org/10.3390/polym13101635.
Costa, A., Appleton, J., 1999. Chloride penetration into concrete in marine environment—Part I: main parameters affecting chloride penetration. Mater. Struct. 32, 252–259. https://doi.org/10.1007/BF02479594.
Cuenca, E., Mezzena, A., Ferrara, L., 2021a. Synergy between crystalline admixtures and nano-constituents in enhancing autogenous healing capacity of cementitious composites under cracking and healing cycles in aggressive waters. Construct. Build. Mater. 266, 121447 https://doi.org/10.1016/j.conbuildmat.2020.121447.
Cuenca, E., Rigamonti, S., Gastaldo Brac, E., Ferrara, L., 2021b. Crystalline admixture as healing promoter in concrete exposed to chloride-rich environments: experimental study. J. Mater. Civ. Eng. 33, 04020491 https://doi.org/10.1061/(ASCE)MT.1943-5533.0003604.
Danner, T., Hjorth Jakobsen, U., Geiker, M.R., 2019. Mineralogical sequence of self-healing products in cracked marine concrete. Minerals 9, 284. https://doi.org/10.3390/min9050284.
De Belie, N., Van Belleghem, B., Erşan, Y.Ç., Van Tittelboom, K., 2019. Durability of self-healing concrete. MATEC Web of Conferences 289, 01003. https://doi.org/10.1051/matecconf/201928901003.
De Weerdt, K., Justnes, H., Geiker, M.R., 2014. Changes in the phase assemblage of concrete exposed to sea water. Cem. Concr. Compos. 47, 53–63. https://doi.org/10.1016/j.cemconcomp.2013.09.015.
De Weerdt, K., Lothenbach, B., Geiker, M.R., 2019. Comparing chloride ingress from seawater and NaCl solution in Portland cement mortar. Cement Concr. Res. 115, 80–89. https://doi.org/10.1016/j.cemconres.2018.09.014.
Du, F., Jin, Z., She, W., Xiong, C., Feng, G., Fan, J., 2020. Chloride ions migration and induced reinforcement corrosion in concrete with cracks: a comparative study of current acceleration and natural marine exposure. Construct. Build. Mater. 263, 120099 https://doi.org/10.1016/j.conbuildmat.2020.120099.
EN 12350-5, 2019. Testing Fresh Concrete - Part 5: Flow Table Test. European Committee for Standardization, Brussels, Belgium.
EN 12350-7, 2019. Testing Fresh Concrete - Part 7: Air Content - Pressure Methods. European Committee for Standardization, Brussels, Belgium.
EN 12390-3, Testing Hardened Concrete. Compressive Strength of Test Specimens, 2019. European Committee for Standardization, Brussels, Belgium.
EN 12390-11, 2010. Testing Hardened Concrete - Part 11: Determination of the Chloride Ressitance of Concrete, Unidirectional Diffusion. European Committee for Standardization, Brussels, Belgium.
Erşan, Y.Ç., Van Tittelboom, K., Boon, N., De Belie, N., 2018. Nitrite producing bacteria inhibit reinforcement bar corrosion in cementitious materials. Sci. Rep. 8, 14092 https://doi.org/10.1038/s41598-018-32463-6.
EUROPEAN COMMITTEE FOR STANDARDIZATION, 2019. NBN EN 12350-6. Testing fresh concrete. Density.
Feng, P., Jia, J., Liu, M., Peng, S., Zhao, Z., Shuai, C., 2021. Degradation mechanisms and acceleration strategies of poly (lactic acid) scaffold for bone regeneration. Mater. Des. 210, 110066 https://doi.org/10.1016/j.matdes.2021.110066.
Green-Basilisk, B.V., 2018. Material Safety Data Sheet Concrete Healing Agent – PLA Based (CHA-PLA).
Gruyaert, E., 2011. Effect of Blast-Furnace Slag as Cement Replacement on Hydration, Microstructure, Strength and Durability of Concrete. Ghent University, Belgium.
Han, Y.S., Hadiko, G., Fuji, M., Takahashi, M., 2005. Effect of flow rate and CO2 content on the phase and morphology of CaCO3 prepared by bubbling method. J. Cryst. Growth 276, 541–548. https://doi.org/10.1016/j.jcrysgro.2004.11.408.
He, P., Yu, J., Wang, R., Du, W., Han, X., Gu, S., Liu, Q., 2020. Effect of ion chelator on pore structure, mechanical property and self-healing capability of seawater exposed mortar. Construct. Build. Mater. 246, 118480 https://doi.org/10.1016/j.conbuildmat.2020.118480.
He, S., Wan, Z., Chen, Y., Jonkers, H.M., Schlangen, E., 2023. Microstructural characterization of crack-healing enabled by bacteria-embedded polylactic acid (PLA) capsules. Cem. Concr. Compos. 143, 105271 https://doi.org/10.1016/j.cemconcomp.2023.105271.
Hearn, N., 1998. Self-sealing, autogenous healing and continued hydration: what is the difference? Mater. Struct. 31, 563–567. https://doi.org/10.1007/BF02481539.
Hirao, H., Yamada, K., Takahashi, H., Zibara, H., 2005. Chloride binding of cement estimated by binding isotherms of hydrates. J. Adv. Concr. Technol. 3, 77–84. https://doi.org/10.3151/jact.3.77.
Khan, M.B.E., Shen, L., Dias-da-Costa, D., 2021a. Self-healing behaviour of bio-concrete in submerged and tidal marine environments. Construct. Build. Mater. 277, 122332 https://doi.org/10.1016/j.conbuildmat.2021.122332.
Khan, M.B.E., Shen, L., Dias-da-Costa, D., 2021b. Self-healing behaviour of bio-concrete in submerged and tidal marine environments. Construct. Build. Mater. 277, 122332 https://doi.org/10.1016/j.conbuildmat.2021.122332.
Kušter Marić, M., Ožbolt, J., Balabanić, G., 2020. Reinforced concrete bridge exposed to extreme maritime environmental conditions and mechanical damage: measurements and numerical simulation. Eng. Struct. 205, 110078 https://doi.org/10.1016/j.engstruct.2019.110078.
Li, V.C., Herbert, E., 2012. Robust self-healing concrete for sustainable infrastructure. J. Adv. Concr. Technol. 10, 207–218. https://doi.org/10.3151/jact.10.207.
Lo Monte, F., Ferrara, L., 2020. Tensile behaviour identification in Ultra-High Performance Fibre Reinforced Cementitious Composites: indirect tension tests and

back analysis of flexural test results. Mater. Struct. 53, 145. https://doi.org/10.1617/s11527-020-01576-8.
Lopez-Calvo, H.Z., Montes-García, P., Jiménez-Quero, V.G., Gómez-Barranco, H., Bremner, T.W., Thomas, M.D.A., 2018. Influence of crack width, cover depth and concrete quality on corrosion of steel in HPC containing corrosion inhibiting admixtures and fly ash. Cem. Concr. Compos. 88, 200–210. https://doi.org/10.1016/j.cemconcomp.2018.01.016.
Lv, L.-S., Wang, J.-Y., Xiao, R.-C., Fang, M.-S., Tan, Y., 2021. Chloride ion transport properties in microcracked ultra-high performance concrete in the marine environment. Construct. Build. Mater. 291, 123310 https://doi.org/10.1016/j.conbuildmat.2021.123310.
Maes, M., 2015. Combined Effects of Chlorides and Sulphates on Cracked and Self-Healing Concrete in Marine Environments. Ghent University, Belgium.
Mangat, P.S., Ojedokun, O.O., 2020. Free and bound chloride relationships affecting reinforcement cover in alkali activated concrete. Cem. Concr. Compos. 112, 103692 https://doi.org/10.1016/j.cemconcomp.2020.103692.
Mehta, P.K., 1991. Concrete in the Marine Environment, first ed. CRC Press.
Mehta, P.K., 1999. Sulfate attack in marine environment. In: Marchand, J., Skalny, J. (Eds.), Sulfate Attack Mechanism, Materials. The American Ceramic Society, westerville, OH, pp. 295–300.
Mohammed, T.U., Otsuki, N., Hamada, H., 2003. Corrosion of steel bars in cracked concrete under marine environment. J. Mater. Civ. Eng. 15, 460–469. https://doi.org/10.1061/(ASCE)0899-1561(2003)15:5460.
Montes, P., Bremner, T.W., Lister, D.H., 2004. Influence of calcium nitrite inhibitor and crack width on corrosion of steel in high performance concrete subjected to a simulated marine environment. Cem. Concr. Compos. 26, 243–253. https://doi.org/10.1016/S0958-9465(03)00043-X.
Mors, R., Jonkers, H.M., 2020. Bacteria-based self-healing concrete: evaluation of full scale demonstrator projects. RILEM Technical Letters 4, 138–144. https://doi.org/10.21809/rilemtechlett.2019.93.
Munyao, O.M., Thiong'o, J.K., Wachira, J.M., Mutitu, D.K., Murithi, G., Mwirichia, R., 2020. Chloride ingress in cement mortars exposed to acidithiobacillus thiooxidans bacteria. Adv. Mater. Sci. Eng. 2020, 1–10. https://doi.org/10.1155/2020/4191806.
Nasser, A., Esmail, R., Abbas, R., Sorour, N., 2022. Effect of Bacillus megaterium bacteria and different calcium source on strength and permeation properties of concrete. ERJ. Engineering Research Journal 45, 401–412. https://doi.org/10.21608/erjm.2022.129257.1157.
NT Build 443, 1995. Concrete, Hardened: Accelerated Chloride Penetration. Nordtest., Finland.
Oliveira, A. de S., Toledo Filho, R.D., de Moraes Rego Fairbairn, E., de Oliveira, L.F.C., da Fonseca Martins Gomes, O., 2022. Microstructural characterization of self-healing products in cementitious systems containing crystalline admixture in the short- and long-term. Cem. Concr. Compos. 126, 104369 https://doi.org/10.1016/j.cemconcomp.2021.104369.
Otieno, M., Beushausen, H., Alexander, M., 2016. Chloride-induced corrosion of steel in cracked concrete – Part I: experimental studies under accelerated and natural marine environments. Cement Concr. Res. 79, 373–385. https://doi.org/10.1016/j.cemconres.2015.08.009.
Palin, D., Wiktor, V., Jonkers, H.M., 2015. Autogenous healing of marine exposed concrete: characterization and quantification through visual crack closure. Cement Concr. Res. 73, 17–24. https://doi.org/10.1016/j.cemconres.2015.02.021.
Palin, D., Wiktor, V., Jonkers, H., 2017. A bacteria-based self-healing cementitious composite for application in low-temperature marine environments. Biomimetics 2, 13. https://doi.org/10.3390/biomimetics2030013.
Pontes, C.V., Réus, G.C., Araújo, E.C., Medeiros, M.H.F., 2021. Silver nitrate colorimetric method to detect chloride penetration in carbonated concrete: how to prevent false positives. J. Build. Eng. 34, 101860 https://doi.org/10.1016/j.jobe.2020.101860.
Ramezanianpour, A.A., Pourkhorshidi, A.R., Sobhani, J., Moodi, F., 2021. Durability of concrete containing blended cements in harsh marine environments: 18 years exposure study. Construct. Build. Mater. 299, 123863 https://doi.org/10.1016/j.conbuildmat.2021.123863.
Rodríguez, C.R., de Mendonça Filho, F.F., Mercuri, L., Gan, Y., Rossi, E., Anglani, G., Antonaci, P., Schlangen, E., Šavija, B., 2020. Chemo-physico-mechanical properties of the interface zone between bacterial PLA self-healing capsules and cement paste. Cement Concr. Res. 138, 106228 https://doi.org/10.1016/j.cemconres.2020.106228.
Roig-Flores, M., Moscato, S., Serna, P., Ferrara, L., 2015. Self-healing capability of concrete with crystalline admixtures in different environments. Construct. Build. Mater. 86, 1–11. https://doi.org/10.1016/j.conbuildmat.2015.03.091.
Roig-Flores, M., Pirritano, F., Serna, P., Ferrara, L., 2016. Effect of crystalline admixtures on the self-healing capability of early-age concrete studied by means of permeability and crack closing tests. Construct. Build. Mater. 114, 447–457. https://doi.org/10.1016/j.conbuildmat.2016.03.196.
Rossi, E., Roy, R., Copuroglu, O., Jonkers, H.M., 2022. Influence of self-healing induced by polylactic-acid and alkanoates-derivates precursors on transport properties and chloride penetration resistance of sound and cracked mortar specimens. Construct. Build. Mater. 319, 126081 https://doi.org/10.1016/j.conbuildmat.2021.126081.
Santhanam, M., Otieno, M., 2016. Deterioration of concrete in the marine environment. In: Marine Concrete Structures. Elsevier, pp. 137–149. https://doi.org/10.1016/B978-0-08-100081-6.00005-2.
Skalny, J., Marchand, J., Odler, I., 1999. Sulfate Attack on Concrete. E & F N Spon, London.
Sumranwanich, T., Tangtermsirikul, S., 2004. A model for predicting time-dependent chloride binding capacity of cement-fly ash cementitious system. Mater. Struct. 37, 387–396. https://doi.org/10.1007/BF02479635.
Tambunan, T., Juki, MohdI., Othman, N., 2019. Mechanical properties of sulphate reduction bacteria on the durability of concrete in chloride condition. MATEC Web of Conferences 258, 01024. https://doi.org/10.1051/matecconf/201925801024.
Tsuji, H., Nakahara, K., 2002. Poly(L-lactide). IX. Hydrolysis in acid media. J. Appl. Polym. Sci. 86, 186–194. https://doi.org/10.1002/app.10813.
Van Belleghem, B., 2018. Effect of Capsule-Based Self-Healing on Chloride Induced Corrosion of Reinforced Concrete. Ghent University, Belgium. PhD Thesis.
Verbeck, G.J., 1975. Mechanisms of Corrosion of Steel in Concrete, 49. ACI Symposium Publication. https://doi.org/10.14359/17530.
Wu, J., Wei, J., Huang, H., Hu, J., Yu, Q., 2020. Effect of multiple ions on the degradation in concrete subjected to sulfate attack. Construct. Build. Mater. 259, 119846 https://doi.org/10.1016/j.conbuildmat.2020.119846.
Wu, Z., Zhang, J., Xu, W., Ding, Y., Ren, Q., Sun, Q., Zhu, Y., 2023. Development of cementitious capillary crystalline waterproofing agents and durability study of concrete in the presence of chloride with sulfate in aqueous environment. J. Build. Eng. 79, 107798 https://doi.org/10.1016/j.jobe.2023.107798.
Xue, C., 2022a. Performance and mechanisms of stimulated self-healing in cement-based composites exposed to saline environments. Cem. Concr. Compos. 129 https://doi.org/10.1016/j.cemconcomp.2022.104470.
Xue, C., 2022b. Cracking and autogenous self-healing on the performance of fiber-reinforced MgO-cement composites in seawater and NaCl solutions. Construct. Build. Mater. 326, 126870 https://doi.org/10.1016/j.conbuildmat.2022.126870.
Yi, Y., Zhu, D., Guo, S., Zhang, Z., Shi, C., 2020. A review on the deterioration and approaches to enhance the durability of concrete in the marine environment. Cem. Concr. Compos. 113, 103695 https://doi.org/10.1016/j.cemconcomp.2020.103695.
Yuan, Q., 2009. Fundamental Studies on Test Methods for the Transport of Chloride Ions in Cementitious Materials. Ghent University.
Zhan, Q., Dong, W., Fu, C., Wang, A., Yi, H., Pan, Z., 2022. The self-healing of marine concrete cracks based on the synergistic effect of microorganisms and inorganic minerals. J. Build. Eng. 61, 105210 https://doi.org/10.1016/j.jobe.2022.105210.
Zhang, Y., Liu, L., Wei, G., Lai, L., 2023. Investigating the self-healing performance of cracked undersea constructions. J. Build. Eng. 80, 107928 https://doi.org/10.1016/j.jobe.2023.107928.
Zhao, G., Li, J., Shi, M., Cui, J., Xie, F., 2020. Degradation of cast-in-situ concrete subjected to sulphate-chloride combined attack. Construct. Build. Mater. 241, 117995 https://doi.org/10.1016/j.conbuildmat.2019.117995.
Zhou, S., Sokolov, A., Lavrentovich, O.D., Aranson, I.S., 2014. Living liquid crystals. Proc. Natl. Acad. Sci. USA 111, 1265–1270. https://doi.org/10.1073/pnas.1321926111.